A unique subset of glycolytic tumor propagating cells drives squamous cell carcinoma

Jee-Eun Choi[1,2], Carlos Sebastian[1,2,#], Christina M. Ferrer[1,2], Caroline A. Lewis[3], Moshe Sade-Feldman[1,4], Thomas LaSalle[1,4], Anna Gonye[1,4], Begona G. C. Lopez[5], Walid M. Abdelmoula[5], Michael S. Regan[5], Murat Cetinbas[6,7], Gloria Pascual[8,9], Gregory R. Wojtkiewicz[10], Giorgia G. Silveira[1,2], Ruben Boon[1,2], Kenneth N. Ross[11], Itay Tirosh[12], Srinivas V. Saladi[1, &], Leif W. Ellisen[1], Ruslan I. Sadreyev[6,7], Salvador Aznar Benitah[8,9], Nathalie Y. R. Agar[5,13,14], Nir Hacohen[1,4], and Raul Mostoslavsky*[1,2,4]

[1]The Massachusetts General Hospital Cancer Center, Harvard Medical School, Boston, Massachusetts 02114, USA
[2]The MGH Center for Regenerative Medicine, Harvard Medical School, Boston, Massachusetts 02114, USA
[3]The Whitehead Institute for Biomedical Research, Cambridge MA 02139, USA
[4]The Broad Institute of Harvard and MIT, Cambridge MA 02142, USA
[5]Department of Neurosurgery, Brigham and Women's Hospital, Harvard Medical School, Boston, MA 02115, USA
[6]Department of Molecular Biology, Massachusetts General Hospital, Boston, MA 02114, USA
[7]Department of Pathology, Massachusetts General Hospital and Harvard Medical School, Boston, MA 02114, USA
[8]Institute for Research and Biomedicine (IRB) Barcelona, The Barcelona Institute of Science and Technology (BIST), Barcelona 08028, Spain
[9]Catalan Institution for Research and Advanced Studies (ICREA), Barcelona 08010, Spain

[10]Center for Systems Biology, Massachusetts General Hospital and Harvard Medical School, Boston, MA 02114, USA
[11]The Dana Farber Cancer Institute, Harvard Medical School, Boston, MA 02115, USA
[12]Department of Molecular Cell Biology, Weizmann Institute of Science, 7610001 Rehovot, Israel
[13]Department of Radiology, Brigham and Women's Hospital, Harvard Medical School, Boston, Massachusetts 02115, USA
[14]Department of Cancer Biology, Dana-Farber Cancer Institute, Harvard Medical School, Boston, Massachusetts 02115, USA

#Present Address: Candiolo Cancer Institute-FPO, IRCCS, Candiolo 10060, Italy
&Present Address: The Massachusetts Eye and Ear Infirmary, Boston, MA 02114 USA

* Correspondence should be addressed to rmostoslavsky@mgh.harvard.edu

ABSTRACT

Head and Neck Squamous Cell Carcinoma (HNSCC) remains among the most aggressive human cancers. Tumor progression and aggressiveness in SCC are largely driven by Tumor Propagating Cells (TPCs). Aerobic glycolysis, also known as the Warburg Effect, represents a characteristic of many cancers, yet whether this adaptation is functionally important in SCC, and at which stage, remains poorly understood. Here, we show that the NAD+-dependent histone deacetylase Sirtuin 6 (SIRT6) is a robust tumor suppressor in SCC, acting as a modulator of glycolysis in these tumors. Remarkably, rather than a late adaptation, we find enhanced glycolysis specifically in TPCs. More importantly, using single cell RNA sequencing of TPCs, we identify a subset of TPCs with higher glycolysis and enhanced pentose phosphate pathway and glutathione metabolism, characteristics that are strongly associated with a better antioxidant response. Altogether, our studies uncover enhanced glycolysis as a main driver in SCC, and, more importantly, identify a subset of TPCs as the cell-of-origin for the Warburg effect, defining metabolism as a key feature of intra-tumor heterogeneity.

56

57

58

59

60

61

INTRODUCTION

Tumor propagating cells (TPCs or cancer stem cells) in squamous cell carcinoma (SCC) are responsible for sustaining primary tumors and are able to re-populate the entire tumor after transplantation due to their self-renewal and differentiation capacity[1]. As such, TPCs have emerged as attractive therapeutic targets[2]. Although genetic drivers, such as the surface marker CD34 and the transcription factor SOX2[3-6] have been identified in TPCs, the specific metabolic characteristics of these cells remain poorly investigated.

Metabolic reprogramming has emerged as a critical hallmark of cancer[7,8]. In particular, increased glycolysis and lactate production under normoxia (aerobic glycolysis) represent one of the best-described characteristics of many tumors. Such an adaptation, also known as the Warburg effect, provides transformed cells with intermediate metabolites for biomass, while balancing cellular redox status for continuous proliferation[9,10]. SIRT6, a member of the NAD^+-dependent protein deacylases known as sirtuins, negatively regulates HIF-1α-dependent glycolysis gene expression (e.g. the glucose transporter GLUT1, pyruvate dehydrogenase kinase 1 (PDK1), and lactate dehydrogenase-A (LDHA) as an H3K9/H3K56 deacetylase,

affecting glucose homeostasis[11,12]. *Sirt6*-deficient cells exhibit aggressive tumor formation through enhanced aerobic glycolysis in colon cancer[13], and increased expression of oncofetal proteins in pancreatic cancer[14], emphasizing a pivotal role for SIRT6 in glucose metabolism and tumorigenesis.

In this study, we find that enhanced glycolysis in a model of SIRT6 loss enriches for $CD34^+$ TPCs, in turn resulting in a much more aggressive tumorigenic phenotype. Mechanistically, highly glycolytic $CD34^+$ TPCs present a distinct gene signature associated with glutathione (GSH) metabolism and stemness, thereby providing a defense against oxidative stress, which is robustly enhanced upon *Sirt6* loss. Using metabolite profiling analysis, we further demonstrate that generation of antioxidants and nucleotides through the oxidative phase of the pentose phosphate pathway (oxPPP) is largely responsible for the aggressive tumorigenic phenotype. Remarkably, direct metabolite measurement from *in vivo* tumor samples in cellular spatial resolution by MALDI-Mass Spectrometry Imaging (MSI) indicates higher glycolysis and more reduced GSH in $CD34^+$ TPCs compared to $CD34^-$ tumor cells. Further, single cell RNA-sequencing (scRNA-seq) analysis defines a subset of TPCs with such characteristics that are functionally crucial for TPC enrichment and tumorigenic

potential. Our studies provide the first in-depth characterization of the metabolic adaptations in SCC, identifying a previously unrecognized metabolic heterogeneity within TPCs, a key feature to support antioxidant protection and nucleotide synthesis in these unique tumor-driving cells.

RESULTS

SIRT6 acts as a tumor suppressor in SCC by modulating aerobic glycolysis

We sought to define an *in vivo* model of squamous cell carcinoma (SCC) to closely examine the effect of increased glycolysis in tumorigenesis and its specific subpopulations including TPCs. We reasoned whether SIRT6 could act as a tumor suppressor in squamous cell carcinoma, one of the major types of epithelial cancers, via modulation of glycolysis. Notably, SIRT6 copy number loss is associated with shorter overall survival when analyzed in patient samples of HNSCC in The Cancer Genome Atlas (TCGA, Extended Data Fig. 1a). Further, both *SIRT6* copy number and expression were significantly decreased in HNSCC compared to matched normal tissue in either the Oncomine or the TCGA (Extended Data Fig. 1b-c). *SIRT6* expression was already observed in early-stage tumors, implicating that *SIRT6* loss

114 may be functionally important in both initiation and maintenance of SCCs (Extended
115 Data Fig. 1b). We next analyzed SIRT6 protein expression in human HNSCC patient
116 samples and normal skin tissues by immunohistochemistry and found that less
117 differentiated tumors tend to have less SIRT6 expression (Extended Data Fig. 1d).
118 Lastly, among available human cancer cell lines listed in the Cancer Cell Line
119 Encyclopedia (CCLE), almost all HNSCC cell lines (denoted as Upper aerodigestive
120 tract) exhibited *SIRT6* loss (Extended Data Fig. 1e). Altogether, these analyses suggest
121 a potential tumor suppressive role for *SIRT6* in SCC.

122 In order to better define the roles of *Sirt6* in squamous cell carcinogenesis, we
123 generated an *in vivo Sirt6* conditional knockout (cKO) mouse model (*Sirt6 F/F; K14-*
124 *cre+*) that specifically deletes *Sirt6* in the skin epithelium. These mice along with wild
125 type (WT) animals (*Sirt6 +/+; K14-cre+*) were treated with DMBA (7,12-
126 dimethylbenz[*a*]anthracene), a known carcinogen, followed by repetitive TPA (12-O-
127 tetradecanoylphorbol-13-acetate) treatment for 14 weeks, a well-established protocol
128 to recapitulate SCC *in vivo* (Fig. 1a). Remarkably, *Sirt6*-deficient animals showed an
129 earlier onset of tumors (Fig. 1b) and significantly larger tumors at 14 weeks after
130 DMBA treatment (Fig. 1c). C57BL/6 strain is known to be highly resistant to

tumorigenesis *in vivo*, and without continuous TPA treatment existing skin tumors tend to regress[15]. Consistently, most of the WT tumors became smaller and regressed after discontinuing TPA treatment for more than 7 weeks. In contrast, multiple *Sirt6*-deleted tumors remained and even grew larger (Fig. 1d). Notably, fully transformed SCC were exclusively form in *Sirt6*-deleted animals (Extended Data Fig. 2a). We next assessed tumor cell proliferation and detected a major increase in $PCNA^{+}$ cells in *Sirt6*-deficient tumors (Fig. 1e). Overall, these data suggest that loss of *Sirt6* promotes tumor cell proliferation, resulting in enhanced tumor progression and maintenance.

To directly determine whether increased glycolysis plays a functional role in driving tumor progression, we next administered an inhibitor of glycolysis, dichloroacetate (DCA), in drinking water during the DMBA/TPA treatment *in vivo* (Fig. 1f). Inhibition of glycolysis significantly reduced tumor size in *Sirt6*-deficient animals (Fig. 1g), while continuous inhibition of glycolysis following TPA withdrawal completely impaired the progression of the existing tumors in *Sirt6*-deleted animals (Fig. 1h). These findings emphasize a critical role for aerobic glycolysis in SCC growth and maintenance. Molecularly, dysplastic proliferating cells started to express high

148 levels of GLUT1, while normal proliferating (PCNA+) keratinocytes and hair follicular
149 stem cells (HFSCs) barely expressed GLUT1, suggesting that increased glycolytic
150 metabolism as an important adaptation of transformed cells, not normal proliferating
151 cells (Extended Data Fig. 2b). In line with these results, RNA expression of *Glut1* and
152 another glycolytic gene, *Ldha*, was also increased in tumors compared to adjacent
153 normal skin (Extended Data Fig. 2c). Further, GLUT1 appeared specifically expressed
154 in tumors, particularly in tumor basal layers, compared to normal adjacent skin (Fig.
155 1i, and Extended Data Fig. 2d, left panels). This was also true for the PDK-dependent
156 phosphorylated form of PDH (pyruvate dehydrogenase complex) (Fig. 1i, and
157 Extended Data Fig. 2d, middle panels), the rate-limiting enzyme that converts
158 pyruvate into acetyl-CoA for usage in the TCA cycle. Phosphorylation of PDH
159 inactivates the enzyme, forcing production of lactate instead. Mitochondria pyruvate
160 carrier 1 (MPC1) expression was higher in more differentiated tumor cells compared
161 to basal tumor cells (Extended Data Fig. 2d, right panels), suggesting less pyruvate
162 entry to mitochondria in these cells. These results together indicate that tumor basal
163 cells are exquisitely glycolytic.

We next analyzed expression of SIRT6 and glycolytic genes in samples from patients' squamous cell carcinomas. Several glycolytic genes were inversely correlated with the level of *SIRT6*, a phenotype observed even at early stages of carcinogenesis (Extended Data Fig. 2e). Lastly, SIRT6 low, less differentiated tumors tend to express ubiquitously higher levels of GLUT1 (Extended Data Fig. 2f). This further strengthens our mouse data and validates this *in vivo* model as highly relevant to human HNSCC.

Increased glycolysis by *Sirt6* loss enriches the number of TPCs

Next, we sought to follow these GLUT1$^+$ tumor cells and to assess their functional role in tumorigenesis. First, we analyzed the differentiation state of the GLUT1$^+$ cells in the tumors by using keratin5 and keratin10, markers of basal progenitors and differentiated cells in skin, respectively. Most of the GLUT1$^+$ cells co-stained with keratin5 and were mutually exclusive with keratin10 (Extended Data Fig. 3a), suggesting that less differentiated cells are particularly glycolytic. We next stained for the surface marker CD34, an established marker of TPCs. As expected, most of CD34$^+$ cells co-expressed keratin 5 and were negative for keratin 10 (Extended Data Fig. 3b). Remarkably, most of the GLUT1$^+$ cells were CD34$^+$ and SOX9$^+$, supporting the idea

that glycolytic basal cells are putative TPCs (Fig. 2a, left panels). Importantly, $CD34^+/SOX9^+$ hair follicle stem cells (HFSCs) were $GLUT1^-$, indicating that specifically the $CD34^+$ tumor cells, rather than normal skin stem cells, benefit from enhanced glucose uptake (Fig. 2a, right panels). This is further strengthened by co-staining with GLUT1, CD34, and keratin10 in whole tumor samples and subsequent calculation of correlation values (Extended Data Fig. 3c). Similarly, α6 $integrin^{high}/CD34^+$ have much higher expression levels of GLUT1 compared to α6 $integrin^{high}/CD34^-$ (Extended Data Fig. 3d).

Although markers used to identify TPCs in human HNSCC remain controversial, TPCs in murine cutaneous SCC have been well defined in the past decade[3-6,16-19]. We attempted to analyze and prospectively isolate TPCs (α6 $integrin^{high}/CD34^+$) from *Sirt6* WT or *Sirt6*-deleted skin tumors (Extended Data Fig. 4a). Strikingly, when we analyzed the percentage of TPCs in live lineage-selected (PI^-/YFP^+) tumor cells (see Methods), we found that *Sirt6*-deleted tumors exhibited a significant increase in TPCs (Fig. 2b, and Extended Data Fig. 4b), especially in tumors that were large (more than 2.5 mm in size), compared to size-matched tumors from WT mice. We next inhibited glycolysis *in vivo* by treating the animals with DCA, which caused significantly

198 decreased blood lactate and reduced phospho-PDH (S293) levels (Extended Data Fig.
199 4c-d), both results confirming successful inhibition of glycolysis. More importantly,
200 DCA treatment severely reduced the percentage of TPCs both in WT and *Sirt6*-
201 deficient tumors (Fig. 2c, and Extended Data Fig. 4b), suggesting that enhanced
202 glycolysis could provide a unique advantage to TPCs, a phenotype exacerbated in the
203 absence of SIRT6. All together, these results indicate that the increased tumor growth
204 and maintenance phenotype observed in *Sirt6*-deleted tumors could be due to an
205 increase in TPCs, a population uniquely glycolytic.
206
207 **TPCs exhibited higher glutathione metabolism and better antioxidant response**
208 In order to pinpoint mechanistic pathways that could explain the benefit of
209 enhanced glycolysis in TPCs, we performed RNA-sequencing (Extended Data Fig. 4e-
210 f). First, we established a "common TPC gene signature". In this analysis, we identified
211 397 commonly upregulated genes and 191 commonly downregulated genes (Fig. 2d,
212 and Supplementary Table 1). DAVID pathway analysis in these upregulated genes
213 from DEGs (differentially expressed genes) of *Sirt6* cKO TPC vs *Sirt6* cKO $\alpha6^{high}$/$CD34^{-}$
214 (Supplementary Table 2) and DEGs of WT TPC vs WT $\alpha6^{high}$/$CD34^{-}$ (Supplementary

215 Table 3) revealed upregulation of several pathways in TPCs, including glutathione
216 metabolism, lipid metabolism, amino acid transport, and multicellular organism
217 development (Fig. 2e, and Extended Data Fig. 4g). Some of the commonly
218 upregulated genes were already known to be important in TPCs (e.g. *Sox2*, *Ptk2*,
219 *Ereg*, etc), providing support to the quality of our data[5,6,16,17].

220 Enhanced glutathione metabolism is important for antioxidant defense, and lipid
221 metabolism and amino acid transport are vital for cellular energy and biomass,
222 suggesting that rewiring metabolism is pivotal in TPCs. Consistently, *Sirt6*-deficient
223 TPCs exhibited higher expression of genes in glycolysis and the pentose phosphate
224 pathway (PPP), consistent with their aggressive phenotype (Supplementary Table 4;
225 Fig. 2f, left). Moreover, genes involved in both glutathione metabolism and redox
226 balance, which were enriched in TPCs, were even higher in *Sirt6* cKO TPCs (Fig. 2f,
227 right). Strikingly, genes involved in stemness and carcinogenesis were expressed at a
228 much higher level in *Sirt6*-deleted TPCs compared to WT TPCs, providing further
229 rationale for the increased aggressiveness in the *Sirt6*-deleted tumors (Extended Data
230 Fig. 4h).

231

Increased oxPPP, generation of reduced glutathione (GSH) and nucleotides in SCC

To gain further insights into the metabolic adaptations that can be regulated by SIRT6, we took advantage of two human SCC cell lines. In HSC2 cells that barely express SIRT6, we find that ectopic expression of SIRT6 causes repression of glycolytic gene expression, reduced H3K9/K56 acetylation (Extended Data Fig. 5a), and decreased glycolytic reserve capacity (Extended Data Fig. 5b). Using stable isotope tracing with U-^{13}C-glucose, we found diminished glycolytic flux towards glycolytic intermediates including fructose-6-phosphate (F6P), pyruvate and lactate (Fig. 3a, upper panel, and Extended Data Fig. 5c), and delayed 13C incorporation into ribose-5-phospohate (R5P) (Fig. 3a, middle panel), at a time when most of the cells (both in WT and H133Y) are alive (Extended Data Fig. 5d). Of note, although citrate labeling didn't reach steady state, the flux into citrate from glycolysis via acetyl-CoA (M+2) showed similar labeling kinetics (Extended Data Fig. 5e, left panel). In addition, the flux into α-KG from glycolysis (M+2) that reached a pseudo steady state was not affected, indicating that cells sustain normal mitochondrial respiration (Extended Data Fig. 5e, right panel). Decrease in glycolysis from SIRT6 overexpression was dependent

249 on SIRT6 enzymatic activity, since expression of the SIRT6 H133Y catalytically inactive
250 mutant (HY) did not influence glycolysis (Fig. 3a-b, and Extended Data Fig. 5a-c).
251 Although these experiments suggest that the enzymatic activity of SIRT6 is necessary,
252 we cannot rule out additional, non-enzymatic roles for SIRT6 in this phenotype.

253 The PPP consists of an oxidative phase (critical to regenerate GSH) and a non-
254 oxidative phase, which can be distinguished with 1,2-^{13}C-glucose (depicted in Fig. 3b,
255 upper right panel). Interestingly, the relative fraction of M+1 R5P was appreciably
256 decreased when SIRT6 was overexpressed, while the relative fraction of M+2 R5P
257 remained similar, indicating that the oxidative arm of the PPP was majorly affected
258 (Fig. 3b, middle panel). In addition, sedoheptulose-7-phosphate (S7P), one of the
259 intermediates in the non-oxidative PPP, did not show a notable difference in ^{13}C
260 incorporation (Fig. 3a-b, bottom panels), further confirming our findings. Lastly, ^{13}C
261 incorporation into DNA (M+5 isotopologue) was significantly reduced in these cells
262 (S6WT), indicating that enhanced PPP in SIRT6 deficient tumors serves as a critical
263 precursor in *de novo* nucleotide synthesis (Fig. 3c) (Pool size data is available in
264 Supplementary Table 5).

265 As a complementary approach, we used SCC13, a skin SCC cell line that
266 endogenously expresses high levels of SIRT6. We observed that inducible knockdown

267 of SIRT6 caused increased glycolytic gene expression, increased bulked H3K56Ac, and
268 increased H3K9 acetylation specifically in glycolytic genes (Extended Data Fig. 6a-b).
269 Consistently, a global increase in H3K56Ac is also observed in *in vivo* tumor samples
270 from *Sirt6* cKO animals compare to WT animals (Extended Data Fig. 6c). Intriguingly,
271 $CD34^+$ TPCs in WT tumor samples showed higher H3K56Ac levels compared to $CD34^-$
272 tumor cells, indicating that SIRT6 activity might be reduced in $CD34^+$ TPCs, likely
273 contributing to the enhanced glycolytic phenotype in TPCs (Extended Data Fig. 6d).
274 Knockdown of SIRT6 also boosted glucose uptake (consumption), lactate secretion,
275 and glycolytic capacity (Extended Data Fig. 6e-i), while enriching for the relative
276 abundance of several glycolytic intermediates including pyruvate and lactate
277 (Extended Data Fig. 6l). These results are indicative of a quantitative increase in
278 glucose metabolism and glycolysis, rather than an imbalance between glycolysis and
279 mitochondrial respiration, since the ratios of lactate secretion/glucose consumption
280 and NAD+/NADH did not show differences (Extended Data Fig. 6h and 6j). Notably,
281 highly glycolytic cells (shSIRT6) exhibited more GSH and less GSSG/GSH (oxidized vs
282 reduced forms of glutathione) and lower ROS (Fig. 3d, Extended Data Fig. 6k). We
283 also observe increased levels of several nucleotides and their precursors, consistent

284 with what we observed in HSC2 cells (Extended Data Fig. 6m) (Pool size data is
285 available in Supplementary Table 5). Inhibition of SIRT6 as a driver of metabolic
286 rewiring seems critical for tumor survival and growth, since prolonged overexpression
287 of SIRT6 caused apoptosis of these HSC2 tumor cells, (Extended Data Fig. 7a), while
288 knockdown of SIRT6 in the SCC13 human line enhanced proliferation *in vitro*
289 (Extended Data Fig. 7b), a phenotype inhibited by DCA. We next assessed whether
290 SIRT6 inhibition could impair human tumor growth *in vivo*. For this purpose, we took
291 advantage of an *in vivo* model where the tumor cells are co-injected with tumor
292 associated fibroblasts (TAFs) and human primary keratinocytes (HPKs). Strikingly,
293 SIRT6 knockdown in SCC13 cells significantly increased tumor growth *in vivo*
294 (Extended Data Fig. 7c-e).

295 **Enhanced antioxidative response in glycolytic, CD34$^+$ TPCs**

296 We then sought to directly analyze metabolite levels of CD34$^+$ TPCs from *in vivo*
297 tumors by utilizing Matrix-Assisted Laser Desorption/Ionization Fourier Transform Ion
298 Cyclotron Resonance Mass-Spectrometry Imaging (MALDI FT-ICR MSI), which
299 provides direct evidence about metabolic characteristics of TPCs[20,21]. We used high
300 spatial (25um) and spectral resolution to map the metabolic profiling directly on

301 frozen tumor sections, preserving their structure and histology. A global view of the
302 whole tumors using this cutting-edge technique already distinguish clear metabolic
303 heterogeneity (Extended Data Fig. 8a-b); t-Distributed Stochastic Neighbor
304 Embedding (t-SNE) analysis of all MALDI-MSI peaks along with H&E staining of the
305 same tissue sections created "metabolic images" with almost anatomic precision, in
306 both its ability to separate tumors from adjacent tissues, and to depict metabolic
307 heterogeneity within each tumor. To identify TPCs within these tumor samples,
308 neighboring sections were stained with CD34, as a TPC marker, GLUT1, as a glycolysis
309 marker, and Keratin10, as a differentiated suprabasal cell marker (Fig. 3f, left panels).
310 By using a non-linear transformation algorithm to co-register the two images
311 (MALDI-MSI and IF) from the sequential sections, we were able to appreciate relative
312 abundance of specific metabolites in different tumor subpopulations.

313 Glucose-6-phosphate (G6P), one of the earliest glycolysis intermediates, and
314 citrate, one of the mitochondrial TCA cycle intermediates, both of which yielded
315 robust signals in MALDI-MSI were used to determine relative glycolytic activity within
316 a tumor (Fig. 3e and Extended Data Fig. 8c-g). In general, signals from G6P and
317 citrate showed weak correlation value (below 0.3). Importantly, mean abundance (or

intensity) of G6P was significantly higher in $CD34^+$ cells, while that of citrate was significantly lower in $CD34^+$ cells when compared to $CD34^-$ cells (Extended Data Fig. 8c-g), strongly indicating increased glycolytic activity in $CD34^+$ TPCs compared to non-TPCs. In this regard, reduced glutathione levels were much higher in $CD34^+$ cells (Fig. 3f), consistent with what we observed in highly glycolytic cells by *in vitro* metabolite profiling, further strengthening our finding that TPCs specifically increase glycolysis and PPP for glutathione generation. To functionally assess whether glycolytic TPCs exhibit antioxidant properties, we checked the cellular redox state by using malonyldialdehyde (MDA), a marker of lipid peroxidation, along with SOX2, a TPC marker, in *Sirt6*-deficient skin tumors. Significantly, the two markers exhibited a mutually exclusive staining pattern, further indicating that an important reason for the metabolic rewiring in TPCs is to protect against oxidative stress (Fig. 3g).

scRNA-seq characterizes a subset of TPCs with higher glycolysis and antioxidant response, responsible for tumor progression

Our t-SNE analysis provided evidence for metabolic heterogeneity within TPCs (Fig. 4a and Extended Data Fig. 8h). In order to determine in more detail whether

335 indeed CD34^{+} TPCs exhibit metabolic heterogeneity, we took advantage of single cell
336 RNA sequencing (scRNA-seq). Dimensionality reduction analyses using both UMAP
337 (Uniform Manifold Approximation and Projection) and t-SNE, and principal
338 component analysis separated TPCs of the WT2 sample from all the other TPCs,
339 indicating that TPCs of the WT2 are qualitatively different from those of the other
340 three (Extended Data Fig. 9a-d). Based on tumor size and TPC enrichment, the WT2
341 sample was the smallest and the least aggressive tumor, suggesting that this tumor
342 was likely regressing (as we observed with most of the WT tumors), and thus we
343 decided to exclude TPCs of WT2 in the analysis.

344 Dimensionality reduction analyses of TPCs from the other three samples showed
345 that TPCs of each sample nicely mixed together regardless of sample identity
346 (Extended Data Fig. 9e-f), generating four distinct clusters among TPCs with
347 differentially expressed marker genes (Fig.4b-c, and Supplementary Table 6). Analysis
348 of Stemness and pro-differentiation program (see gene lists in Supplementary Table
349 7) revealed that two distinct clusters, cluster I and IV, showed the highest stemness
350 score and the lowest pro-differentiation score at comparable levels, implying that
351 these are the most stem-like cells (Fig. 4d and Extended Data Fig. 9g-h). Based on

352 gene expression, cluster III might represent contamination of differentiating, CD34^{low}
353 cells during the prospective isolation by FACS, showing clearly less stemness markers
354 and higher pro-differentiation scores with *Sprr1a/b* expression (Fig. 4c-d and
355 Extended Data Fig. 9g-h). We then compared cluster I and IV, separated by
356 differences in their whole transcriptome while presenting similar stemness features.
357 Remarkably, even within these two seemingly identical stem cell clusters (based on
358 stem cell markers), cluster I exhibited significantly higher expression of genes
359 involved in glycolysis, PPP, antioxidant response and glutathione metabolism
360 compared to cluster IV (Fig. 4e; see gene lists in Supplementary Table 7), defining,
361 with unprecedented resolution, metabolically distinct subsets within *bona fide* TPCs.
362 Notably, trajectory analysis in a pseudotime scale strongly suggests that even though
363 cells in the cluster IV may represent the earliest progenitors in SCC, cells in the
364 cluster I, equally stem-like as in the cluster IV, could be the major contributors to
365 aggressive SCC, in part due to their high glycolytic metabolism and ability to
366 generate glutathione (Extended Data Fig. 9i-j).
367
368 **Redox regulation is critical for TPC enrichment and tumor progression**

In order to define whether increase GSH plays a functional role in TPCs, we administered an antioxidant, N-acetyl-cysteine to animals treated with DCA *in vivo*. Strikingly, depleted $CD34^+$ TPCs were completely rescued by exogenous antioxidant administration both in WT and *Sirt6* cKO tumors (Fig. 4f and Extended Data Fig. 10a). To confirm these results, we grew *in vitro* WT and shSIRT6 SCC13 cells in suspension, an approach that select for cancer stem cell activity, as analyzed by tumorsphere formation. Indeed, we saw a 4-fold increase in tumorspheres in shSIRT6 cells, a phenotype abolished by DCA treatment, and fully rescued upon addition of NAC (Fig. 4g and Extended Data Fig. 10b).

Lastly, we took advantage of a dataset from a recent single cell transcriptomic analyses of ten different human HNSCC samples[22], and assessed glycolysis and antioxidant response gene expression. Highly glycolytic tumors (as defined by a "glycolysis score", see Methods) exhibit a robust co-expression signature of antioxidant response genes (as defined by an "antioxidant gene score") (Fig. 4h and Extended Data Fig. 10c-d). This positive correlation seems more obvious in the classical subtype of HNSCC, but not much in the atypical or basal subtypes of HNSCC that barely express glycolytic genes (Extended Data Fig. 10c-d). Furthermore,

386 at a single cell transcriptome level within each classical subtype of HNSCC (MEEI20 &
387 MEEI6), the relationship between glycolysis and antioxidant response gene expression
388 showed a significant positive correlation (Fig. 4h). These analyses from this
389 independent human RNA-seq data further strengthen our findings that increased
390 glycolysis and thus enhanced antioxidant response may promote squamous cell
391 carcinogenesis, especially through TPCs.
392
393 **DISCUSSION**
394 The Warburg effect is considered a late adaptation of rapidly proliferating
395 advanced tumors, yet several descriptive studies indicated that such adaptation may
396 occur early, with increased glycolysis and its branched metabolic pathways (e.g.
397 serine/glycine metabolism) shown to be important specifically in tumor-initiating cells
398 in lung, brain, and breast cancer models[23,2425-27]. In this study, using both genetically
399 engineered mouse models and human SCC lines where glycolytic metabolism was
400 manipulated, we provide direct evidence for a driving role of glycolysis in TPCs, a
401 phenotype regulated at least in part by epigenetic mechanisms. As such, our data
402 represents the first comprehensive analysis that metabolic reprogramming to

403 increase glycolysis is critical for nucleotide biosynthesis and antioxidative functions in
404 TPCs, thus identifying TPCs as the cell-of-origin for the Warburg effect in SCC.
405 Importantly, despite exhibiting a Warburg phenotype (increased glucose uptake, and
406 increased glycolytic flux towards the PPP and lactate production), they appeared to
407 maintain robust mitochondrial respiration, something that has been appreciated in
408 several other cancer types[28].

409 In cutaneous SCC, quiescent, TGFβ-responding SCC stem cells have an increased
410 expression of genes in glutathione metabolism and redox balance, providing cisplatin
411 resistance and tumor recurrence[18]. In our study, we discovered that a subpopulation
412 of highly proliferating $CD34^+$ TPCs showed an augmented antioxidant response and
413 nucleotide biosynthesis via increasing glycolysis, defining a metabolic mechanism to
414 explain the ability of these cells to drive tumorigenesis. Recent studies have shown
415 that both quiescent and proliferative TPCs, regardless of their proliferation states,
416 exhibit elevated gene expression of the antioxidant response genes, including
417 glutathione metabolism genes, though most observations were *in vitro*, lacking *in*
418 *vivo* relevance and evidence from direct measurements of metabolites[19]. Our study
419 defined a subset of TPCs as exhibiting increased GSH and provided strong *in vivo*

data for the importance of increased glycolysis in generating glutathione and defending against oxidative stress. We further discovered a unique "metabolic heterogeneity" within TPCs, indicating that only a defined (previously unknown) subpopulation of $CD34^+$ TPCs acquires metabolic adaptations that could drive tumorigenesis. Our studies add metabolism to the large list of heterogeneous traits that have emerged in recent years in cancer cells[29]. These results may open a new therapeutic opportunity to target this specific subpopulation of TPCs in SCC by modulating glucose metabolism, in turn providing new hope for patients with these aggressive tumors for which treatment remains a challenge.

Acknowledgements

We thank David Lombard for the pTripZ-shSIRT6 construct, Martina Weissenboeck for pMSCV-luc-PGK-Neo-IRES-eGFP construct, Cyril Benes for the HSC2 cell line and Paolo Dotto for the SCC13 cell line. We also thank Ben Berman, Howard Cedar and Tiago Silva for providing the analysis on SIRT6 promoter methylation, and Carlos Villacorta-Martin for providing advice on scRNA-seq analysis. We would like to thank all the members of the Mostoslavsky lab for helpful discussions and critical reading

437 of the manuscript. We also thank the Flow core facilities at the MGH Cancer for
438 Regerative medicine and at the MGH Department of Pathology. C.S. was supported
439 by the Department of Defense Visionary Postdoctoral Award (CA120342) and he is
440 the recipient of the Marie Sklodowska-Curie Actions Individual Fellowship (EF-RI).
441 R.M. is the Laurel Schwartz Endowed Chair in Oncology. This work was supported by
442 NIH grants R01CA175727 and R01GM128448 (R.M), and the Arthur, Sandra and Sarah
443 Irving Fund for Gastrointestinal Immuno-Oncology (N.H.).

444

445 **Authors' contributions**

446 J-E.C. and R.M. conceptualized and designed the study; J-E.C. performed and
447 analyzed most of the experiments; J-E.C., C.S., and C.M.F. performed animal
448 experiments; C.A.L. performed and analyzed LC-MS metabolite assays; M.S-F., T.L.,
449 A.G., performed and analyzed scRNA-sequencing with supervision of N.H.; B.G.C.L.,
450 W.M.A., and M.S.R. performed and analyzed MALDI-MSI with supervision of N.Y.R.A.;
451 M.C. and R.I.S. performed and analyzed bulk RNA-sequencing; G.P. and S.A.B.
452 designed xenotransplantation assays; G.R.W. performed and analyzed
453 bioluminescence imaging; J-E.C. and G.G.S. performed and analyzed

454 immunofluorescence imaging and western blot assays; R.B. performed and analyzed
455 GC-MS assays; K.N.R. analyzed the TCGA data; I.T. analyzed scRNA-seq data from
456 human HNSCC patient samples; S.V.S. and L.W.E. provided FFPE human samples for
457 immunohistochemical analysis; J-E.C. and R.M. wrote the manuscript; R.M. supervised
458 the project.

459

460 **Competing Interests Statement**

461 R.M has a financial interest in Galilei Biosciences Inc, a company developing
462 activators of the mammalian SIRT6 protein. R.M.'s interests were reviewed and are
463 managed by MGH and MGB HealthCare in accordance with their conflict of interest
464 policies. N.H. has equity in BioNtech and Related Sciences. N.Y.R.A. is a key opinion
465 leader to Bruker Daltonics. The other authors declare no competing interests.

466

467 **References**

468 1. Visvader, J. E. & Lindeman, G. J. Cancer Stem Cells: Current Status and Evolving
469 Complexities. *Cell Stem Cell* **10,** 717–728 (2012).
470 2. Frank, N. Y., Schatton, T. & Frank, M. H. The therapeutic promise of the cancer
471 stem cell concept. *J. Clin. Invest.* **120,** 41–50 (2010).
472 3. Malanchi, I. *et al.* Cutaneous cancer stem cell maintenance is dependent on β-
473 catenin signalling. *Nature* **452,** 650–653 (2008).

4. Lapouge, G. E. L. *et al.* Skin squamous cell carcinoma propagating cells increase with tumour progression and invasiveness. *The EMBO Journal* **31,** 4563–4575 (2012).
5. Boumahdi, S. *et al.* SOX2 controls tumour initiation and cancer stem-cell functions in squamous-cell carcinoma. *Nature* **10,** 246–250 (2014).
6. Siegle, J. M. *et al.* SOX2 is a cancer-specific regulator of tumour initiating potential in cutaneous squamous cell carcinoma. *Nature Communications* **5,** 127 (2014).
7. Hanahan, D. & Weinberg, R. A. Hallmarks of Cancer: The Next Generation. *Cell* **144,** 646–674 (2011).
8. Pavlova, N. N. & Thompson, C. B. The Emerging Hallmarks of Cancer Metabolism. *Cell Metabolism* **23,** 27–47 (2016).
9. Vander Heiden, M. G., Cantley, L. C. & Thompson, C. B. Understanding the Warburg Effect: The Metabolic Requirements of Cell Proliferation. *Science* **324,** 1029–1033 (2009).
10. Warburg, O. On the Origin of Cancer Cells. *Science* **123,** 309–314 (1956).
11. Kugel, S. & Mostoslavsky, R. Chromatin and beyond: the multitasking roles for SIRT6. *Trends in Biochemical Sciences* **39,** 72–81 (2014).
12. Zhong, L. *et al.* The Histone Deacetylase Sirt6 Regulates Glucose Homeostasis via Hif1a. *Cell* **140,** 280–293 (2010).
13. Sebastian, C. *et al.* The Histone Deacetylase SIRT6 Is a Tumor Suppressor that Controls Cancer Metabolism. *Cell* **151,** 1185–1199 (2012).
14. Kugel, S. *et al.* SIRT6 Suppresses Pancreatic Cancer through Control of Lin28b. *Cell* **165,** 1401–1415 (2016).
15. Abel, E. L., Angel, J. M., Kiguchi, K. & DiGiovanni, J. Multi-stage chemical carcinogenesis in mouse skin: Fundamentals and applications. *Nature Protocols* **4,** 1350–1362 (2009).
16. Beck, B. *et al.* A vascular niche and a VEGF–Nrp1 loop regulate the initiation and stemness of skin tumours. *Nature* **478,** 399–403 (2011).
17. Schober, M. & Fuchs, E. Tumor-initiating stem cells of squamous cell carcinomas and their control by TGF-β and integrin/focal adhesion kinase (FAK) signaling. *Proc Natl Acad Sci USA* **108,** 10544–10549 (2011).
18. Oshimori, N., Oristian, D. & Fuchs, E. TGF-β Promotes Heterogeneity and Drug Resistance in Squamous Cell Carcinoma. *Cell* **160,** 963–976 (2015).

19. Brown, J. *et al.* TGF-β-Induced Quiescence Mediates Chemoresistance of Tumor-Propagating Cells in Squamous Cell Carcinoma. *Cell Stem Cell* **21,** 650–664.e8 (2017).
20. Randall, E. C. *et al.* Localized Metabolomic Gradients in Patient-Derived Xenograft Models of Glioblastoma. *Cancer Research* **80,** 1258–1267 (2020).
21. Swales, J. G. *et al.* Quantitation of Endogenous Metabolites in Mouse Tumors Using Mass-Spectrometry Imaging. *Anal. Chem.* **90,** 6051–6058 (2018).
22. Puram, S. V. *et al.* Single-Cell Transcriptomic Analysis of Primary and Metastatic Tumor Ecosystems in Head and Neck Cancer. *Cell* **171,** 1611–1624.e24 (2017).
23. Lunt, S. Y. & Vander Heiden, M. G. Aerobic Glycolysis: Meeting the Metabolic Requirements of Cell Proliferation. *Annu. Rev. Cell Dev. Biol.* **27,** 441–464 (2011).
24. Hsu, P. P. & Sabatini, D. M. Cancer Cell Metabolism: Warburg and Beyond. *Cell* **134,** 703–707 (2008).
25. Zhang, W. C. *et al.* Glycine Decarboxylase Activity Drives Non-Small Cell Lung Cancer Tumor-Initiating Cells and Tumorigenesis. *Cell* **148,** 259–272 (2012).
26. Mao, P. *et al.* Mesenchymal glioma stem cells are maintained by activated glycolytic metabolism involving aldehyde dehydrogenase 1A3. *Proc Natl Acad Sci USA* **110,** 8644–8649 (2013).
27. Feng, W. *et al.* Targeting Unique Metabolic Properties of Breast Tumor Initiating Cells. *Stem Cells* **32,** 1734–1745 (2014).
28. DeBerardinis, R. J. & Chandel, N. S. We need to talk about the Warburg effect. *Nat Metab* **2,** 127–129 (2020).
29. Almendro, V., Marusyk, A. & Polyak, K. Cellular heterogeneity and molecular evolution in cancer. *Annu Rev Pathol* **8,** 277–302 (2013).

Figure Legends

Figure 1. *Sirt6* acts as a tumor suppressor in squamous cell carcinoma by negatively regulating aerobic glycolysis. a, DMBA/TPA-induced skin carcinogenesis

539 protocol in *Sirt6* WT or *Sirt6* cKO animals. **b,** Tumor-free period after starting DMBA
540 treatment in *Sirt6* WT or *Sirt6* cKO animals. Statistical analysis was done by log-rank
541 test. **c,** Tumor size was measured at 14 weeks after DMBA treatment. Data are
542 presented as mean ±S.D. **d,** Tumor progression was assessed after stopping TPA
543 treatment (at 14 weeks post DMBA) for least 7 weeks. Fisher's exact test was
544 performed for statistical analysis ($p<0.0001$, two-sided). **e,** PCNA immunostaining in
545 DMBA/TPA-treated skin tumors from *Sirt6* WT or *Sirt6* cKO animals. Representative
546 images (lower panel, scale bars indicate 100μm) and quantification of $PCNA^+$ layers
547 from normal adjacent skin and skin tumors (upper panel). **f,** Schematic presentation
548 of DCA treatment in DMBA/TPA-treated animals. DCA was administered at 7-8 weeks
549 after DMBA treatment, in order to avoid any confounding effect of DCA on tumor
550 initiation. **g,** Tumor size was measured at 14 weeks after DMBA treatment. Data are
551 presented as mean ±S.D. **h,** Tumor progression was assessed after stopping TPA
552 treatment with continuous DCA treatment. Data of the first two groups shown in
553 Figure 1d were used again for comparison. Fisher's exact test was performed for
554 statistical analysis ($p<0.0001$, two-sided). **i,** GLUT1 and phospho-PDH (Ser293)
555 immunostaining in *Sirt6*-deleted large papilloma samples. Scale bars indicate 100μm.

Statistics, sample sizes (n) and numbers of replications are presented in Methods, 'Statistics and reproducibility'. * $p<0.05$, ** $p<0.01$, *** $p<0.001$

Figure 2. Increased glycolysis enriches for tumor-propagating cells *in vivo*. a, Immunofluorescence images against GLUT1, CD34, and SOX9 in *Sirt6*-deficient tumors and normal epidermis. Images were acquired by a Leica SP8 white light confocal microscope. Scale bars indicate 50μm. **b & c,** Representative FACS plots to analyze and isolate tumor-propagating cells (α6 integrin^{high}/CD34^{+}) from *Sirt6* WT or *Sirt6*-deleted skin tumors without DCA **(b)** or with DCA **(c)**. **d,** DAVID pathway analysis (GOTERM_BP_DIRECT) of 397 commonly upregulated genes in TPCs from differentially expressed genes (DEGs) between TPCs and α6^{high}/CD34^{-} cells in each genotype. **e & f,** Representative gene list and corresponding fold changes in expression from *Sirt6* WT or cKO TPCs and its negative counterparts (α6^{high}/CD34^{-}) for functional gene categories associated with each biological process. Data indicate mean. Statistics, sample sizes (n) and numbers of replications are presented in Methods, 'Statistics and reproducibility'.

Figure 3. Glycolytic TPCs uniquely upregulate glutathione metabolism via the oxidative PPP to mitigate oxidative stress. a & b, Relative enrichment of fully

573 labeled metabolic intermediates after incubation with U-^{13}C-glucose **(a)** or 1,2-^{13}C-
574 glucose **(b)** at a given time point either in SIRT6 WT or H133Y overexpressing HSC2
575 cells (26hr post doxycycline). Data are presented as mean ±S.D. **c,** ^{13}C incorporation
576 into DNA from U-^{13}C-glucose via ribose-5-phosphate (M+5) at 24hr either in SIRT6
577 WT or H133Y overexpressing HSC2 cells (26hr post doxycycline). Data are presented
578 as mean ±S.D. **d,** A relative abundance of GSH and a relative ratio of GSSG/GSH
579 either in control (shCtrl) or *SIRT6* knockdown (shSIRT6) SCC13 cells 3 days post
580 doxycycline. Data is from at least two biological replicates (n=2 for shCtrl and n=3
581 for shSIRT6). Data are presented as mean ±S.E.M. **e,** Co-registration images (the left
582 two) of G-6-P and citrate on top of immunofluorescence image (CD34 and GLUT1) in
583 tumor 2. Overlay image (the very right) of G-6-P and citrate with a correlation value
584 of distribution between two metabolites. Scale bars indicate 300μm **f,**
585 Immunofluorescence image against CD34, GLUT1, and Keratin10 (left panels) and
586 MALDI-MSI (glutathione) from DMBA/TPA-treated skin tumors (middle panels), and
587 box plots to compare glutathione abundance between different tumor
588 subpopulations (right panels). Scale bars indicate 300μm **g,** Immunohistochemical
589 analysis against malonyldialdehyde (MDA), a lipid peroxidation marker and SOX2, a

functional TPC marker in the same tumor samples (serially sectioned). Scale bars indicate 100μm. Statistics, sample sizes (n) and numbers of replications are presented in Methods, 'Statistics and reproducibility'. * $p<0.05$, ** $p<0.01$, *** $p<0.001$

Figure 4. A subset of TPCs that are glycolytic supports glutathione metabolism and antioxidant response, functionally critical for TPC enrichment and tumorigenic potential *in vivo*. a, A tSNE image of MALDI-MSI only with $CD34^+$ cells **b,** Dimensionality reduction analysis (UMAP (resolution 0.5) and tSNE) of prospectively isolated $CD34^+$ TPCs (1 WT tumor and 2 *Sirt6* cKO tumors) **c,** A heatmap showing top 5 differentially expressed genes in each cluster **d,** Cd34 and a6 integrin expression levels in UMAP graphs (the very left), and violin plots (right two) showing stemness and pro-differentiation program score in each cluster **e,** Violin plots showing glycolysis, pentose phosphate pathway (PPP), antioxidant response, and glutathione metabolism program score in the cluster I and IV **f,** Representative FACS plots to analyze and isolate tumor-propagating cells ($\alpha6$ $integrin^{high}/CD34^+$) from *Sirt6* WT or *Sirt6*-deleted skin tumors with DCA (top) or with DCA and NAC (bottom). DCA treatment plots in the top are the same as the ones in Fig. 2C. **g,** The number of tumorspheres at day 10 in SCC13 cells in indicated conditions. Data

607 indicate mean ±S.E.M. **h,** Scatter plot of glycolysis score and antioxidant gene
608 signature score in single cells of two classical subtypes of HNSCC with a linear
609 regression. Pearson correlation coefficients are $2.7e^{-48}$ for MEEI20 and $6.2e^{-06}$ for
610 MEEI6, respectively. Statistics, sample sizes (n) and numbers of replications are
611 presented in Methods, 'Statistics and reproducibility'. * $p<0.05$, ** $p<0.01$, ***
612 $p<0.001$

613 **METHODS**

614 **Mice and chemical-induced skin carcinogenesis** Mice were housed in pathogen-
615 free facilities. All experiments were conducted under the protocol 2019N000111
616 approved by the Subcommittee on Research Animal Care at Massachusetts General
617 Hospital. Mice were maintained as a highly pure C57BL/6 background (> 96%).
618 Unless indicated, all animals were maintained under a standard diet (Prolab Isopro
619 RMH 3000, Cat. #0006972). Data presented include both male and female mice. *Sirt6*
620 *F/F* conditional strain[13] were crossed with the *K14-cre* strain (Jackson laboratory). For
621 flow cytometry analysis, these animals were further crossed with *ROSA26-LSL-EYFP*
622 (Jackson laboratory). Two days after shaving their back hairs, 8-week-old mice were
623 subject to a one time DMBA (Sigma, 200 nmol in acetone) treatment followed by

TPA (Sigma, 20 nmol in acetone) treatment three times a week for 14 weeks. After 14 weeks of DMBA/TPA treatment, some mice were kept without TPA treatment for at least 7 weeks to observe tumor progression. The appearance and the number of tumors were closely monitored twice a week. Any visible mass that was more than 1 mm in size and existed for more than a week was considered as a tumor for onset and counting numbers of tumors. Some of the DMBA/TPA-treated animals were administered with DCA (Acros Organics, 5 g/L) and/or N-acetyl cysteine (Sigma, 1g/L) in their drinking water. N-acetyl cysteine containing water was changed every week due to stability of this drug in aqueous solution. Blood from tail vein was collected into EDTA-coated tubes. Plasma was separated by centrifugation (15000 rpm, 10min, 4°C) for further analysis.

For the analysis and prospective isolation of TPCs, we generated *K14-cre+; Sirt6 F/F; ROSA26-LSL-YFP* (*Sirt6* cKO) animals as well as *Sirt6* WT (*K14-cre+; Sirt6 +/+; ROSA26-LSL-YFP*) animals to specifically isolate YFP^+ epithelial cells by FACS. In addition, because we had difficulty obtaining sizable WT tumors with the previous DMBA/TPA treatment protocol, we modified the protocol by treating mice with TPA

for more than 24 weeks in order to obtain sufficient number of cells to perform sub-population analysis.

Humane Endpoint: for all tumors' assays, animals were euthanized according to IACUC protocol (tumors reached 20mm, ulcerated mass, or loss of 15% weight).

Human data sets *SIRT6* expression and copy number, and glycolytic gene expression data were obtained from the Oncomine[30] and the Cancer Cell Line Encyclopedia[31]. *SIRT6* copy number and the corresponding survival of each patient data were obtained from the The Cancer Genome Atlas[32]. A Kaplan-Meier plot was made and the log-rank p-value was calculated for the *SIRT6* copy number in the TCGA HNSC samples. TCGA HNSC clinical information was downloaded from the TCGA data matrix access portal (http://cancergenome.nih.gov) during December 2015 and GISTIC2 processed copy number data for TCGA HNSC was downloaded from the Broad Institute (http://gdac.broadinstitute.org) during April 2015. Follow-up clinical data files were merged with the original clinical data file to ensure that the most up-to-date patient follow-up information was used for survival analysis. The Kaplan-Meier survival plot and the log-rank p-value were generated using R with the 522 TCGA HNSC primary tumor samples with both clinical data with a death event or at

657 least six months of follow-up and GISTIC2 copy number data available. Kaplan-Meier
658 plots used overall survival with death from any cause as the endpoint and patients
659 still alive at last follow-up were censored at last follow-up time. Samples were split
660 into 5 groups based upon the GISTIC2 data for SIRT6 in the
661 all_thresholded.by_genes.txt results file (a gene-level table of discrete amplification
662 and deletion indicators at for all samples). Within the GISTIC2 table, values of 0
663 means no amplification or deletion above the threshold (0.1) while positive numbers
664 represent amplifications and negative numbers represent deletions (1 means
665 amplification above the amplification threshold, 2 means amplifications larger than
666 any arm-level amplifications observed for the sample, -1 represents deletion beyond
667 the threshold, -2 means deletions greater than the minimum arm-level deletion
668 observed for the sample).
669 **Human tumor sample analysis** Primary HNSCC tumors and newborn baby foreskins
670 (used as normal tissue in this study) analyzed in this study were collected following
671 institutional IRB approval. The collection and use of discarded, de-identified tissue
672 was reviewed and approved by the Dana-Farber/Harvard Cancer Center IRB (Protocol

673 #03-204). Briefly, tissues were fixed in formalin followed by ethanol and paraffin
674 embedded followed by serial sectioning onto slides for IHC.

675 **Histology and immunostaining** Mouse back skin and skin tumors were harvested,
676 submitted for histological examination, and analyzed in a blinded fashion by a
677 pathologist (Dr. Roderick Bronson) at the DF/HCC Research Pathology Core. Tissue
678 samples were fixed overnight in 10% buffered formalin, and then embedded in
679 paraffin and sectioned 5μm thickness by the DF/HCC Research Pathology Core.
680 Hematoxylin and eosin staining was performed using standard methods.
681 Immunohistochemistry was performed as previously described with modifications[33]. In
682 brief, deparaffinization, rehydration, and antigen retrieval were performed in
683 unstained slides with Trilogy solution (Cell Marque). Slides were incubated for 20min
684 with 4% H_2O_2 at RT to block endogenous peroxidase activity and rinsed twice with
685 water. Sections were blocked with 10% goat serum (Cell signaling) in TBS-0.1% tween
686 20 for an hour at RT, and then incubated overnight with primary antibodies at
687 4°C.The following primary antibodies were used: anti-SIRT6 (Cell Signaling, #12486)
688 1:50 for human tissues and 1:100 for mouse tissues, anti-GLUT1 (Abcam, ab40084)
689 1:200 for human and mouse tissues, anti-PCNA (Santa Cruz, sc-56) 1:500 for mouse

690 tissues, anti-phospho-PDH (Abcam, ab92696) 0.1 μg/ml for mouse tissues, anti-MPC1
691 (Sigma, HPA045119) 1:100 for mouse tissues, anti-SOX2 (Abcam, ab92424) 1:50 for
692 mouse tissues, anti-MDA (Abcam, ab6463) 1:1000 for mouse tissues, and anti-CD34
693 (BD sciences, 553731) 1:50 for mouse tissues. Slides were washed three times for
694 10min each in TBST and incubated with biotinylated secondary antibodies (1:200,
695 Vector Laboratories) in blocking solution for 45min at RT, followed by signal
696 detection using Vectastain ABC kit (Vector Laboratories) and DAB substrate kit
697 (Vector Laboratories). Counterstaining was performed with hematoxylin. Stained
698 slides were photographed with an Olympus DP72 microscope or a Leica DM1000
699 microscope. Immunofluorescence staining was performed as previously described
700 with modifications[33]. Briefly, deparaffinization, rehydration, and antigen retrieval were
701 performed in unstained slides with Trilogy solution (Cell Marque). Sections were
702 blocked with 5% goat serum (Cell signaling), 1% BSA (Sigma), and 0.2% gelatin
703 (Sigma) in PBS-0.1% triton-x for an hour at RT, and then incubated overnight with
704 primary antibodies at 4°C. The following primary antibodies were used: anti-GLUT1
705 (Abcam, ab40084) 1:200 for mouse tissues, anti-CD34 (BD sciences, 553731) 1:50 for
706 mouse tissues, anti-SOX9 (Millopore, AB5535) 1:2000 for mouse tissues, anti-

H3K56Ac (Abcam, ab76307) 1:500 for mouse tissues, anti-Keratin 5 (Covance, PRB-160P) 1:1000 for mouse tissues, and anti-Keratin 10 (Covance, PRB-159P) 1:1000 for mouse tissues. Slides were kept in dark containers. Samples were washed three times for 10min each in TBST and incubated with secondary antibodies for 2hr at RT. The following secondary antibodies were used: anti-rabbit, anti-mouse, and anti-rat conjugated to AlexaFluor488 (Molecular Probe, 1:500-1:1000), AlexaFluor595 (Molecular Probe 1:500-1:1000), AlexaFluor647 (Molecular Probe 1:400-1:1000), and rhodamin red-X (Jackson ImmunoResearch, 1:500-1:1000). Stained slides were mounted in the mounting reagent (Vector lab, H-1200) containing DAPI for nuclei staining. Pictures were obtained using a Leica SP8 white light confocal microscope or a Nikon Eclipse Ni-U fluorescence microscope. Quantification of positive/negative cells was done manually using ImageJ.

Real time RT-qPCR analysis Total RNA was extracted with the TriPure isolation reagent (Roche) as described by the manufacturer. For RNA isolation from mouse skin or tumor samples, additional RNA clean up procedure was performed with the RNeasy Protect Mini kit (Qiagen). cDNA synthesis and Real-time PCR were done as previously described[14]. In brief, isolated RNA was reverse transcribed by using the

QuantiTect Reverse Transcription kit (Qiagen). Real-time PCR was performed using SYBR green master mix (Roche) with the final volume of 12.5 μl per reaction in LightCycler 480 detection system (Roche). Data were presented as relative mRNA levels normalized to the β-actin expression level in each sample. The primer sequences are listed in Supplementary Table 8.

Mouse tumor cell isolation and fluorescence-activated cell sorting (FACS) Mice bearing skin tumors were euthanized and the tumors were collected on ice. Each tumor was cut into small pieces and incubated with 0.5% trypsin (diluted in keratinocyte serum-free medium, Gibco) on a horizontal shaker at 37°C for 1.5 hr. Using an 18G syringe, digested tumor cells were physically isolated into a single cell suspension. The trypsin was inactivated by adding chelexed FBS. After serial filtering with 70μm and 40μm strainers (BD sciences), tumor cells were centrifuged at 1200 rpm, 4°C for 10 min. Cell pellets were resuspended with PBS containing 4% chelexed FBS and then transferred into FACS tubes with a 40μm filter. The following fluorophore-conjugated antibodies were used: anti-CD34-BV421 (BD sciences, 562608, 1:50) and anti-CD49f-PE (eBiosciences, 12-0495-81, 1:200), anti-GLUT1-A647 (Abcam, ab195020, 1:100). Propidium iodide (Sigma, P4864, 1:1000) or Zombie NIR

fixable viability dye (Biolegend, 423105, 1:100) were used to negatively select live cells. Proper isotype controls, single color controls, and FMO controls were used in every experiment to set up optimal compensation and gates. Cells were analyzed and sorted using a FACSAria II (BD). Obtained data were analyzed by FlowJo. An exemplary gating strategy is described in Supplementary Information Figure 1.

RNA preparation and RNA sequencing. Following FACS isolation of two different tumor sub-populations ($\alpha6^{high}$/$CD34^{+}$ and $\alpha6^{high}$/$CD34^{-}$) from at least two independent skin tumors obtained from *Sirt6* WT and *Sirt6*-deleted animals, sorted tumor cells were directly collected into RNA isolation buffer provided in the kit (Clontech, #740902.50). RNA isolation was conducted by the manufacturer's instruction. Library construction was performed using the SMART-Seq v4 Ultra Low Input RNA kit to produce cDNA (Clontech, #634888). The total RNA input amount for this kit was 10 ng total. 8 cycles of PCR were performed for PCR amplification. Post cDNA construction, the samples were validated using an Agilent 2100 Bioanalyzer and Agilent's High Sensitivity DNA kit. Prior to generating the final library for Illumina Sequencing, the Covaris AFA system is used to shear cDNA resulting in a 200-500 bp size range. Sheared libraries are validated using Agilent 2100 Bioanalyzer and

758 Agilent's High Sensitivity DNA kit. Quantification was completed by using a Qubit 4
759 fluorometer (Invitrogen) using the Qubit RNA HS Assay kit. Generation of the final
760 library was completed by using Low Input Library Prep Kit v2 (Clontech, #634899).
761 The cDNA input amount was 10 ng total. 7 cycles of PCR were performed for PCR
762 amplification. Post library construction, the samples were validated using the 2200
763 Tapestation System and High Sensitivity D1000 ScreenTape kit. Libraries were
764 quantified using the Library Quantification kit (Kapa Biosystems, #KK4828) and the
765 BioRad CFX96 instrument. Each lane of sequencing was pooled into a 6-plex (6
766 samples per lane) with unique barcodes. Pooled libraries were also quantified using
767 the Kapa Biosystems Library Quantification kit (#KK4828) and the BioRad CFX96
768 instrument. These pools were then denatured to 16pM with 1% phix and sequenced
769 on the Illumina HiSeq2000 instrument, producing approximately 30 million paired-
770 End 50bp reads per sample.

771 **RNA sequencing analysis** STAR aligner[34] was used to map sequencing reads to the
772 mouse reference transcriptome (mm9 assembly). Read counts over transcripts were
773 calculated using HTSeq v.0.6.0[35] based on a current Ensembl annotation file for
774 NCBI37/mm9 assembly. Differential expression analysis was performed using EdgeR[36],

775 genes were classified as differentially expressed based on the cutoffs of at least 2-
776 fold change. Analysis of enriched functional categories among detected genes was
777 performed using DAVID[37].

778 **Cell lines and cell culture** SCC13 cells (a gift from Paolo Dotto, MGH Cutaneous
779 Biology department, USA) were grown in keratinocyte serum-free medium (K-SFM,
780 Gibco) supplemented with EGF (epidermal growth factor) and bovine pituitary extract
781 based on the manufacturer's instruction. HSC2 cells (a gift from Cyril Benes, MGH
782 Cancer Center, USA) were grown in DMEM/F-12 medium with 10% Tet system
783 approved FBS (Clontech) and 1% penicillin (100 U/ml)/streptomycin (100 U/ml)
784 (Gibco). Human primary keratinocytes were obtained from CellnTec and were grown
785 in CnT-PR medium (CellnTec) supplemented with 1% penicillin (100
786 U/ml)/streptomycin (100 U/ml) (Gibco). Human tumor-associated fibroblasts (a gift
787 from Salvador Aznar Benitah, IRB, Spain) were grown in DMEM medium
788 supplemented with 10% FBS (Sigma), Insulin-Transferrin-Selenium reagent (Gibco),
789 and 1% penicillin (100 U/ml)/streptomycin (100 U/ml) (Gibco). All cells were cultured
790 and maintained at 37°C under 5% CO_2. Human primary keratinocytes (Cat. #HPEKp,

791 CellIn Tec), were passaged with accutase (Gibco) and were used within four passages.
792 All the other cell lines were passaged by trypsinization.
793 **Constructs and viral infection** Human pTripZ-shSIRT6 (Dharmacon RHS4740) and
794 negative control shRNA vector were kind gifts from David Lombard (University of
795 Michigan, USA). pMSCV-luc-PGK-Neo-IRES-eGFP construct was a kind gift from
796 Martina Weissenboeck (IMP, Austria). pLVX-Tet-On was obtained from Clontech.
797 Human pRetro-SIRT6 WT and pRetro-SIRT6 H133Y were previously described[17]. Viral
798 particles containing the above-mentioned constructs were generated using either
799 lentiviral (pCMV-d8.9) or retroviral (pCL-ECO) packaging plasmids with pCMV-VSV-G
800 (Addgene) in 293T cells. Virus-containing supernatant was filtered in 0.45 μm filter
801 and added into target cell lines with 8 μg/ml polybrene. For infection of SCC13 cells,
802 filtered virus-containing supernatant was ultra-centrifuged at 20,000 g, 4°C for 2 hr
803 to concentrate into a very small volume (~200 μl) and about 5 μl of virus concentrate
804 was used for infection of SCC13 cells. For efficient infection, 6-well plates with SCC13
805 cells added virus concentrate and polybrene were centrifuged at 2,250 rpm, 32°C for
806 1 hr and virus-containing media were immediately replaced by regular K-SFM. The
807 next day, cells were selected in 2 μg/ml of puromycin, or 1.4 mg/ml of neomycin for

SCC13 cells, or in 1.5 μg/ml puromycin, or 0.5 mg/ml of neomycin for HSC2 cells for at least a week and the pooled populations were used for various experiments. SCC13 cells with dox-inducible pTripZ constructs were treated with 1 μg/ml doxycycline for at least 3 days and HSC2 cells with dox-inducible pRetro constructs were treated with 100 ng/ml doxycycline for 26 hr unless otherwise indicated.

Western blot analysis Whole cell lysates/chromatin fractions were prepared and western blot analysis was performed as previously described[12]. In brief, for chromatin extraction, cell pellets were lysed in buffer containing 10mM HEPES pH7.4, 10mM KCl, 0.05% NP-40 supplemented with a protease inhibitor cocktail (Complete EDTA-free, Roche Applied Science), 5 μM TSA, 5mM sodium butyrate, 1mM DTT, 1mM PMSF, and 0.2mM sodium orthovanadate. After incubation for 20min on ice, the lysates were centrifuged at 14,000 rpm, 10min at 4 °C. The supernatant was removed (cytosolic fraction) and the pellet (nuclei) was acid-extracted using 0.2N HCl by incubating 20min on ice. The lysate was further centrifuged at 14,000 rpm, 10min at 4 °C. The supernatant was neutralized in 1M Tris-HCl pH 8. Protein concentration was determined by Biorad protein assay. Western blots were performed using 8-15% gradient gels (Biorad). Primary antibodies were used as follows: anti-SIRT6 (Cell

825 signaling #12486), anti-H3K9Ac (Millipore, 07-352), anti-H3K56Ac (Abcam, ab76307),
826 anti-total H3 (Abcam, ab1791), anti-GLUT1 (Abcam, ab40084), anti-PDK1 (Cell
827 signaling, #3820), anti-LDHA (Cell signaling, #2012S), anti-phospho-PDH (Abcam,
828 ab92696), and anti-β-actin (Sigma, A5316). All uncropped and unprocessed scans are
829 available in Source Data Figures 1-4.

830 **Glucose uptake assay** In SCC13 cells, cells were plated in duplicates on 6-well plates
831 ($2.5*10^5$ cells/well) in culture medium a day before the experiment. Media containing
832 2-NBDG (Invitrogen, 100 μM) were added for 2 hr. Fluorescence was measured in
833 FACSAria II. Obtained data were analyzed by FlowJo. After proper compensation,
834 geometric mean value was normalized by its negative control (without 2-NBDG) of
835 each group.

836 **Glycolytic capacity** Cells were plated into XFe96 cell culture microplates (Seahorse
837 Bioscience) a day before the experiment. Media were replaced in the Seahorse
838 microplates with assay medium supplemented with 2 mM L-glutamine (Gibco), pH
839 7.35 ± 0.05 for glycolysis stress test. The plate was incubated in a CO_2-free incubator
840 for 1 hr at 37°C. For glycolysis test, 10 mM of glucose, 2 μM of oligomycin, 100 mM
841 of deoxyglucose were sequentially injected. ECAR was measured in every well based

842 on the instrument's protocol. Experiments were run using an XFe96 analyzer and raw
843 data were normalized by cell number calculated with Cyquant cell proliferation assay
844 kit (Thermo scientific).

845 **Chromatin immunoprecipitation** Chromatin immunoprecipitation followed by RT-
846 qPCR was performed as previously described[38] with H3K9Ac (Millipore, 07-352). In
847 brief, SCC13 cells were crosslinked with 1% formaldehyde/PBS for 15miin at RT,
848 followed by quenching with 0.125M glycine. After washing twice with PBS, cells were
849 collected in RIPA buffer, and then were sonicated to generate DNA fragments of
850 approximately 500 bp in size. About 200ug of pre-cleared protein extract was used
851 for immunoprecipitation overnight (>12hr) at 4 °C using protein A/G agarose beads
852 (Santa Cruz, sc2003). Washed samples were eluted by incubation at 65 °C for 10 min
853 with 1% SDS, and crosslinking was reversed by incubation at 65 °C for 6 hr with
854 200mM NaCl. DNA was purified using the QIAquick spin kit (Qiagen) and assessed by
855 real-time qPCR using the LightCycler 480 system (Roche). The primers' sequences are
856 listed in Supplementary Table 9.

857 **Isotope tracing experiment** HSC2 Cells were maintained with doxycycline for 26hr,
858 at which point intracellular metabolites were collected after adding labeled media at

different time points. Glucose-free DMEM/F-12 medium (US biological) was supplemented with 10% dialyzed FBS, 17.5 mM of U-^{13}C-glucose or 1,2-^{13}C-glucose (Cambridge isotope labs), and 15 mM HEPES. SCC13 cells were maintained with doxycycline for 3 days, at which point intracellular metabolites were collected after adding labeled media at different time points. Keratinocyte serum-free medium (Gibco) was supplemented with 5.8 mM of U-^{13}C-glucose (Cambridge isotope labs). At different time points after replenishing labeled media, media from biological triplicates (in 6-well plate) was fully aspirated. Each well was washed with 0.9% ice-cold NaCl twice and 1 ml of 80% (v/v) methanol was added at dry ice temperature. After vigorous vortexing, insoluble material in lysates was centrifuged at 16,000 g, 4°C for 10min. The supernatant was transferred and the solvent was evaporated using a SpeedVac. Samples were stored at -80°C until analyzed.

Metabolite profiling by LC-MS Metabolite profiling and isotope tracing LC/MS analyses were conducted on a QExactive bench top orbitrap mass spectrometer equipped with an Ion Max source and a HESI Ⅱ probe, which was coupled to a Dionex UltiMate 3000 HPLC system (Thermo Fisher Scientific, San Jose, CA). External mass calibration was performed using the standard calibration mixture every 7 days.

876 Typically, samples were reconstituted in 100 µL water and 2 µL were injected onto a
877 SeQuant® ZIC®-pHILIC 150 x 2.1 mm analytical column equipped with a 2.1 x 20
878 mm guard column (both 5 mm particle size; EMD Millipore). Buffer A was 20 mM
879 ammonium carbonate, 0.1% ammonium hydroxide; Buffer B was acetonitrile. The
880 column oven and autosampler tray were held at 25°C and 4°C, respectively. The
881 chromatographic gradient was run at a flow rate of 0.150 mL/min as follows: 0-20
882 min: linear gradient from 80-20% B; 20-20.5 min: linear gradient form 20-80% B;
883 20.5-28 min: hold at 80% B. The mass spectrometer was operated in full-scan,
884 polarity-switching mode, with the spray voltage set to 3.0 kV, the heated capillary
885 held at 275°C, and the HESI probe held at 350°C. The sheath gas flow was set to 40
886 units, the auxiliary gas flow was set to 15 units, and the sweep gas flow was set to 1
887 unit. MS data acquisition was performed in a range of *m/z* = 70–1000, with the
888 resolution set at 70,000, the AGC target at $1x10^6$, and the maximum injection time at
889 20 msec. An additional scan (*m/z* 220-700) in negative mode only was included to
890 enhance detection of nucleotides. Relative quantitation of polar metabolites was
891 performed with XCalibur QuanBrowser 2.2 (Thermo Fisher Scientific) using a 5ppm
892 mass tolerance and referencing an in-house library of chemical standards. For stable

893 isotope tracing analyses, data were corrected for natural abundance[39]. Metabolite
894 pool sizes of the above-mentioned metabolites are described in Supplementary table
895 5.

896 **Lactate measurement by GC-MS** Ice-cold methanol was added into 5 ul of plasma
897 from tail vein blood, vigorously vortexed at 4°C for 10min, followed by centrifugation.
898 The supernatant was transferred and the solvent was evaporated using a SpeedVac.
899 Samples were stored at -80°C until analyzed. Derivatization and measurement on
900 the GC-MS was done as previously described[40]. In brief, polar metabolites were
901 derivatized with 20mg/ml methoxyamine in pyridine for 90min at 37°C and
902 subsequently with N-(tert-butyldimethylsilyl)-N-methyl-trifluorosilane and 1% tert-
903 butyldimethylchlorosilane for 60min at 60°C. Metabolite levels were then measured
904 with a 5977B GC system (Agilent Technologies). The raw ion chromatograms were
905 extracted to determine metabolite levels using a custom Matlab M-file[41].

906 **ROS measurement** Cells were plated in duplicates on 12-well plates ($1*10^5$ cells/well)
907 in culture medium. After 3 days in the presence or absence of doxycycline (1 µg/ml),
908 cells were trypsinized, centrifugated, and resuspended in the media. Cells were

incubated with CellROX deep red (Invitrogen) for 30min at 37°C. Fluorescence was measured in LSRII (BD). Obtained data were analyzed by FlowJo.

Proliferation assay SCC13 cells were pretreated with doxycycline (1 μg/ml) for at least 3 days before plating cells. Cells were plated in triplicates on 6-well plates ($1*10^4$ cells per well) in culture medium with doxycycline in the presence or absence of DCA. Adherent cells were trypsinized and counted by trypan-blue exclusion at 2, 3, 5 days later.

Apoptosis assay Cells were plated in duplicates on 12-well plates ($2.5*10^4$ cells/well) in culture medium. After 4 days in the presence of doxycycline (100 ng/ml), all the floating and adherent cells were collected and stained with Annexin V-FITC (BD sciences) and PI (Sigma) to analyze cell death in Accuri (BD). Obtained data were analyzed by FlowJo.

Skin xenotransplantation assay and bioluminescence imaging SCC13 shCtrl or shSIRT6 cells were stably transduced with retrovirus containing pMSCV-luc-PGK-Neo-IRES-eGFP. After neomycin selection (1.4 mg/ml), infected cells were further sorted with GFP using a FACSAria II (BD) and sorted GFP^{high} cells were cultured before the experiment. 4,000 cells of SCC13 shCtrl or shSIRT6 cells, 1,000 cells of human primary

keratinocytes, and 500 cells of tumor-associated fibroblasts were prepared and mixed immediately before injection. Mixed cells were injected after inserting a silicone chamber (Renner GmbH) in the back skin of NSG mice (Jackson laboratory) under avertin anesthesia. Doxycycline (200 μg/ml) was administered in the drinking water and was replaced every week due to its light sensitivity. After 8 days, the silicone chamber was removed from the back skin of the mice under avertin anesthesia and several sutures were made to aid the wound healing process. All the surgical procedures were performed in the aseptic hood of the pathogen-free facility. Every mouse was singly housed due to the small open-wounded area after silicone chamber removal. From day 23, all the mice were subject to bioluminescence imaging once a week. Under isoflurane anesthesia, 300μl of D-luciferin (15 mg/ml) (RR labs Inc., San Diego, CA) was injected intraperitoneally, and the mice were imaged every 5 min after injection with a 0.5 s to 60 s exposure time with a binning of 8 and 4 on an Ami-X imaging system (Spectral Instruments Imaging, Tucson, AZ) until the total flux and maximal radiance peaked. Total flux (photons/s) and maximal radiance (photons/s/cm^2/sr) were measured by Spectral Ami X (Spectral Instruments Imaging, Tucson, AZ). A region of interest (ROI) was drawn around the tumor region

for each mouse as well as a background ROI outside of the mice of which was subtracted from the total flux and maximum radiance for each mouse.

Humane Endpoint: for all tumors' assays, animals were euthanized according to IACUC protocol (tumors reached 20mm, ulcerated mass, or loss of 15% weight).

3D tumorsphere assay 5 * 10^4 SCC13 cells pretreated with doxycycline for at least 3 days were trypsinized and plated into 24-well ultra-low attachment plates (Corning) with DMEM/F12 media supplemented with 2% B27 (Invitrogen), 0.4% BSA (Sigma), 20 ng/ml EGF (Peprotech), and 4ug/ml Insulin (Sigma). Fresh media with doxycycline were added in every 3 days. The number of tumorspheres was manually counted under a Nikon Eclipse Ni-U microscope at day 10.

MALDI Mass Spectrometry Imaging (MSI) in skin tumors DMBA/TPA-treated skin tumors and adjacent skin samples were collected, snap-frozen in LN_2, and stored at -80°C until analysis. Samples were embedded in a solution of 2% methylcellulose for sectioning in the Microm HM550 cryostat (Thermo Scientific) at 10µm thickness. The cryo-sections were mounted in indium tin oxide (ITO) slides pre-coated with 90% CHCA (5 mg/mL) in acetonitrile for MALDI MSI and consecutive sections were mounted in regular glass slides for immunostaining. The ITO slides were then coated

with 90% 9-aminoacridine (5 mg/mL in acetonitrile) using an automated matrix sprayer (TM-sprayer, HTX imaging, Carrboro, NC) under the following conditions: 4 passes, 0.17 mL/min flow rate, 75°C, 10 psi nitrogen pressure, 1000 mm/min speed. A 9.4T SolariX XR FT-ICR mass spectrometer (Bruker Daltonics, Billerica, MA) with a MALDI source was used to acquire spectra in negative ion mode, with a raster pixel size of 25 μm. The mass range was m/z 60-1500 with continuous accumulation of selected ions was set between m/z 100-520. A tuning mix was used for external calibration in the selected mass range. FlexImaging 5.0 was used for acquiring the images, while Scils 2019c was used for data processing.

Multi-nodal images processing and integration 1) H&E and IF: The H&E and immunofluorescence images were pre-processed[42] to exclude the background noise. These two imaging modalities exhibit local deformations (such as compression and tearing) due to the manual nature of the tissue sectioning process and the underlying different staining procedures. The iterative parametric-based image registration framework was used to non-linearly warp the H&E image to be spatially aligned with immunofluorescence image[43]. The non-linear image registration process was first initialized by Affine transformation to capture global deformations (scaling,

977 rotation, translation, and shearing) and map the images to the same coordinate
978 space. The non-linear transformation model of cubic B-Spline was used to model the
979 local deformations. The cost function of mutual information has been found efficient
980 as a similarity metric for multi-modal registration[44] and it was optimized by the
981 adaptive stochastic gradient descent algorithm[45]. For robustness and faster
982 convergence, the image registration was implemented using a multi-resolution
983 strategy that employed 8-levels of Gaussian smoothing[46]. The registration algorithm
984 was implemented using the publicly available toolbox of elastix[43], and eventually it
985 yields an optimized non-linear transformation model, T_{μ_1}.
986 2) MALDI-MSI and H&E: The complex nature of MSI data pose challenges that hinder
987 direct co-registration with histology. This complexity is described in terms of high
988 dimensionality and the lack of established spatial correspondences between
989 biochemical and anatomical images. We have adopted the t-SNE based non-linear
990 image registration methodology developed by Abdelmoula et al.[47]. Briefly, the t-SNE
991 computes pairwise similarities of the high dimensional datapoints (i.e. spectra) and
992 non-linearly maps it into a lower dimensional embedding of 3-dimensions. The t-SNE
993 non-linearity preserves the local similarity of the higher dimensional datapoints in the

994 embedding space as such similar spectra are projected closely to each other whereas
995 dissimilar ones are projected further away. The embedding features were spatially
996 mapped to form a t-SNE image that reveals structures in which edges demarcate
997 molecularly distinct regions. The t-SNE image was non-linearly aligned to histology
998 using the elastix toolbox[43]. The registration was initialized with Affine transformation
999 to capture linear deformation and then followed by a cubic B-Spline transformation
1000 to capture non-linear deformations. The cost function of mutual information and the
1001 multi-resolution strategy of 4-levels of Gaussian smoothing were used. The resultant
1002 transformation model, T_{μ_2}, was applied to spatially-align a given m/z image to the
1003 histological image, and then be aligned to immunofluorescence image using the
1004 previously computed model T_{μ_1}.
1005 3) ROI and multi-modal correlation: We chose ROIs based on matching histology
1006 between H&E and immunofluorescence slides because they are not the exactly same
1007 slides and also excluded edge and folded areas due to strong auto-fluorescence
1008 signals. In selected ROIs, signal intensities of MALDI-MSI images were quantified
1009 based on the cellular markers defined by immunofluorescence images, using in-
1010 house Matlab codes.

Single cell RNA-sequencing of sorted TPCs Isolation of TPC cells for single cell RNA sequencing was done on a BD Aria cell sorter, by sorting cells into 96 well plates (Eppendorf) containing 10µl of lysis buffer (TCL buffer + 1% 2-mercaptoethanol). Selection of cells was done using standard cell surface staining protocols with BV421-CD34 (BD sciences, 562608, 1:50), PE-CD49f (eBiosciences, 12-0495-81, 1:200), and by gating on endogenous YFP expression in *ROSA26-LSL-eYFP; Keratin14-Cre* transgenic mice. The viability dye propidium iodine (Sigma, P4864, 1:1000) was used to exclude dead cell and was added after antibody labeling.

RNA isolation, and libraries generation was done by using a modified version of the SmartSeq2 protocol as recently described[48]. Briefly, 22µl of Agencourt RNAClean XP SPRI beads (Beckman Coulter, A63987) was added and mixed in the 96 well plates containing sorted single cell lysates. After 10 minutes incubation, plates were placed on a DynaMag-96 side skirted magnet (Invitrogen, 12027) for 5 minutes, followed by supernatant removal and two washes with 75% ethanol. Next, dried beads were mixed with 4µl of mix-1 containing 1µl (10µM) RT primer (IDT, DNA oligo) 5′-AAGCAGTGGTATCAACGCAGAGTACT30VN-3′; 1µl (10mM) dNTPs (Thermo-Fisher, R0192); 1µl (4U/µl) Recombinant RNase Inhibitor (Clontech, 2313B); and 1µl nuclease

free water, and plates were placed in a thermocycler for 3 minutes at 72°C. After RNA denaturation, reverse transcription (RT) step was done by adding, 7µl of mix-2 containing 0.75µl nuclease free water; 2µl 5X Maxima RT buffer (Thermo-Fisher, EP0753); 2µl (5M) betaine (Sigma-Aldrich, B0300-1VL); 0.9µl (100mM) $MgCl_2$ (Sigma-Aldrich, M1028); 1µl (10µM) TSO primer (Qiagen, RNA oligo) 5′-AAGCAGTGGTATCAACGCAGAGTACATrGrG+G-3′; 0.25µl (40U/µl) Recombinant RNase Inhibitor (Clontech, 2313B); and 0.1µl (200U/µl) of Maxima H Minus Reverse Transcriptase (Thermo-Fisher, EP0753) was added and mixed followed by 90 minutes incubation at 50°C and 5 minutes incubation at 85°C. For cDNA amplification, 14µl of mix-3 containing 1µl nuclease free water; 0.5µl (10µM) ISPCR primer (IDT, DNA oligo) 5′-AAGCAGTGGTATCAACGCAGAGT-3′; and 12.5µl 2X KAPA HiFi HotStart ReadyMix (KAPA Biosystems, KK2602) was added and mixed, and plates were placed for 3 minutes at 98°C, followed by 21 cycles at [98°C for 15 seconds, 67°C for 20 seconds and 72°C for 6 minutes] with final extension at 72°C for 5 minutes. Removal of primer dimers after cDNA amplification was done by adding 20µl of Agencourt AMPureXP SPRI beads (Beckman Coulter, A63881) to each well, incubation for 5 minutes, placement of plates on a DynaMag-96 side skirted magnet for 5 minutes,

followed by two 75% ethanol washes and resuspension of dried beads with 20µl TE buffer (Tekanova, T0228). This step was repeated to ensure complete removal of primer dimers. Quantification of the concentration of each cell was done on the Cytation-5 plate reader (BioTek) by using the Qubit dsDNA high sensitivity assay (Invitrogen, Q32854). For each plate, representative wells were also evaluated for cDNA size distribution to ensure quality of sorted cells, using the High-sensitivity DNA Bioanalyzer kit (Agilent 5067-4626). The Nextera XT library Prep kit (Illumina, FC-131-1096) was used to generate libraries for next-generation sequencing. After this step barcoded single cells were grouped into a single tube, followed by sequencing on a NextSeq 500 sequencer (Illumina) using the 75 cycles kit, with paired-end 38-base-reads and dual barcoding 8-base-reads.

Single cell RNA-seq data generation and processing FASTQ files were aligned to the NCBI Genome Reference Consortium Mouse Build 38 (mm10) using STAR[34]. Expression levels were computed using the RSEM tool and quantified as both raw counts and Transcripts Per Million (TPM)[49]. For each cell, we used four quality control (QC) metrics. We excluded: (1) cells expressing less than 2500 genes with three or more counts, (2) cells with less than 500,000 RNA molecules detected, (3) cells with

mitochondrial gene counts exceeding 10% of total gene expression[50], (4) cells with an average expression of housekeeping genes[48], log2(TPM+1) < 6.

Dimensionality reduction The t-Distributed Stochastic Neighbor Embedding (t-SNE) and Uniform Manifold Approximation and Projection (UMAP) methods were used for dimensionality reduction within the Seurat package[51]. The dimensionality of the dataset was determined by Principal Component Analysis (PCA), and the first five principal components (PCs) were used as inputs to the dimensionality reduction.

Unsupervised clustering of tumor cells TPCs were clustered using the R package Seurat v. 3.1.1[51]. The same PCs as in the dimensionality reduction were used as input to the clustering analysis. The resolution parameter was set to 0.5 in order to identify the greatest number of clusters with at least 20 significant marker genes. To be considered a marker gene, the gene must be enriched in the given cluster with a Wilcoxon Rank Sum test Bonferroni-adjusted p-value of less than 0.05 and a minimum log-fold change of 0.25 when comparing the cells of the cluster to all other cells. Statistical analysis was performed in R (version 3.6.1).

Pathway score analyses of TPCs from scRNA-seq For each single cell, we assigned a score for each of several programs based on the average expression of a selected

gene set of interest minus the average of a control gene set, based on the work of Puram, S.V. et al[22]. For glycolysis and glutathione metabolism, we began with a list of relevant genes and calculated the Pearson correlation coefficient between all pairs of genes in the list. We sequentially removed genes with the strongest negative correlations to other genes until all genes were positively correlated in the list. Then, we removed genes with the weakest positive correlations until all pairs of genes had a Pearson correlation coefficient of at least 0.2. For the pentose phosphate pathway and pro-differentiation, we followed a similar process of elimination, but stopped eliminating genes once all correlations were positive, as the correlations were weaker. For stemness, we used a list of genes associated with stemness but did not eliminate any genes due to the genes on the list being largely uncorrelated. For antioxidant response, we ranked the entire list of analyzed genes by their correlation with the NRF2 transcription factor controlling the antioxidant response. We removed unannotated genes to only include genes with known functions, and selected the top 30 positively correlated genes to make the gene list of interest. As described in Puram, S.V. et al., the gene expression levels of a given program may be confounded by the overall complexity of a given cell, since cells with high expression complexity

would be expected to score well for any given pathway. To control for this, the cell score for a given pathway is defined as $SC_j(i)$ = average[Er(G_j,i)] – average[Er(G_j^{cont},i)], where G_j is a given gene set, $SC_j(i)$ is the score of each cell i, and Er is average relative expression. The cell score is then the score of the given pathway in that cell minus the score of a control gene set. The control gene set is selected by dividing all analyzed genes into 25 bins of equal size according to their overall expression, and for each gene in G_j, selecting 100 genes from the same expression bin.

Trajectory analysis of TPCs To analyze the differentiation trajectory of the TPCs based on the single-cell RNA-seq gene expression data, we used Monocle v. 2.13.0[52]. Monocle identified a set of 14,321 differentially expressed genes between the four clusters established in Seurat. These genes were ordered by ascending q-value, and the top 1000 genes were used as input to Monocle's Reversed Graph Embedding algorithm. Branched expression analysis modeling (BEAM) was used to identify genes with branch-dependent expression, and a q-value cutoff of 1e-15 was applied.

Single cell transcriptomic analysis of human HNSCC patient samples We restricted the analysis to malignant cells, as defined previously[22] and scored each cell for each program, based on the average expression of a set of pre-defined genes, minus the

1113 average of a control gene-set (see Puram, S. V. et al. for further description of how
1114 the control scores are selected). For glycolysis, we initially examined the gene
1115 set PDK1, G6PD, PGD, PFKM, LDHB, LDHA. Since five of those genes were all
1116 positively correlated with one another (across single cancer cells) while the sixth
1117 (LDHA) was not correlated it was removed from the list, and the remaining five genes
1118 were used to define final scores. For antioxidant gene score, we first calculated the
1119 correlation of each gene with NRF2 across all cancer cells. We then selected the top
1120 30 genes (including NRF2) to define antioxidant gene score (NRF2) scores. As
1121 expected, this list includes many known downstream targets of NRF2 such as GPX2
1122 and genes associated with detoxification/antioxidants etc.
1123
1124 **Statistics and Reproducibility**
1125 **Figure 1, b,** Statistical analysis was done by log-rank test (p= 0.0176). WT, n=9; cKO,
1126 n=14. **c,** Student's t-test was performed (two-sided). WT, n=34 biologically
1127 independent tumors; cKO, n=36 biologically independent tumors. **d,** Fisher's exact
1128 test was performed for statistical analysis ($p<0.0001$, two-sided). WT, n=7; cKO, n=11.
1129 **e,** (Upper panel) Student's t-test was performed ($p<0.0001$, two-sided). At least 4

different measurements in 2 different microscopic images (40x) from 2 biologically different samples were analyzed for normal skin samples. At least 4 different measurements in 3 different microscopic images (40x) from 3 biologically different samples were analyzed for tumor samples. The number of measurements as follows; WT normal, n=16; cKO normal, n=16; WT tumor, n=34; cKO tumor, n=45. (Lower panel) Immunostaining against PCNA was performed six times with similar results. **g,** Student's t-test was performed (two-sided). WT, n=34 biologically independent tumors; cKO, n=36 biologically independent tumors; WT with DCA, n=28 biologically independent tumors; cKO with DCA, n=43 biologically independent tumors. **h,** Fisher's exact test was performed for statistical analysis ($p<0.0001$, two-sided). WT, n=7; cKO, n=11; WT with DCA, n=4; cKO with DCA, n=4**. i,** Immunostaining against GLUT1 and p-PDH was performed ten and three times, respectively, with similar results.

Figure 2, a, Immunofluorescent staining was performed five times with similar results. **e & f,** Data is from at least two biological replicates (n=3 for WT and n=2 for *Sirt6* cKO), presented by mean.

1146 **Figure 3, a,** Data is from three biological replicates. **b,** Data is from three biological
1147 replicates. **c,** Student's t-test was performed (two-sided). Data is from three biological
1148 replicates. **d,** Student's t-test was performed (two-sided). Data is from at least two
1149 biological replicates (n=2 for shCtrl and n=3 for shSIRT6). **e,** Data is from two
1150 biologically independent tumor samples, consisting of more than hundred thousands
1151 of pixel datapoints per sample. **f,** Immunofluorescence staining was performed two
1152 times with similar results. The nonparametric Wilcoxon rank sum test (two-sided and
1153 95% significance level) was used after checking normality distribution using
1154 Kolmogorov-Smirnov test. Details of the box plots are listed in the Source Data file 1.
1155 **g,** Immunostaining was performed three times with similar results.
1156 **Figure 4, a,** Data is always reproducible every time the code was run. The key point
1157 for this stability is the random seed point in the t-SNE algorithm is set to zero and
1158 that maintained reproducibility. The t-SNE analysis was done on MATLAB 2018a that
1159 was installed on a workstation operating with Windows 10. **d, right panel,** ANOVA
1160 test was performed. F values are as follows: Stemness, F=14.47; Pro-differentiation,
1161 F=95.23. **e,** Pairwise comparisons using t-test were used to calculate p-value (p-value

adjustment was done by BH). **g,** Data is from three biological replicates. Paired student t-test was performed (two-sided).

Extended Data Figure 1, a, Log-rank test was performed. **b & c, left panels,** Student t-tests were performed. Details of the box plots are listed in the Source Data file 2. **d,** Immunostaining was performed two times with similar results.

Extended Data Figure 2, b, Immunostaining was performed ten times for GLUT1 and six times for PCNA with similar results. **c,** Each dot represents one biologically independent tumor sample. (n=1, 2, 6, 5, respectively, from left to right in each graph) Student's t-tests were performed (two-sided). **d,** Immunostaining against GLUT1, p-PDH, and MPC1 was performed ten, three, and two times, respectively, with similar results. **e,** Definitions of each box plot are listed in Source Data file 3. **f,** Immunostaining was performed two times with similar results.

Extended Data Figure 3, a & b, Immunostaining was performed three times with similar results. Quantification is done by at least three independent 20x images with hundreds of positive cells. **c,** Immunostaining was performed two times with similar results.

Extended Data Figure 4, b, Each dot represents one biologically independent tumor sample. (n= 2, 6, 3, 6, 5, 3 respectively, from left to right in each graph) Student's t-tests were performed (two-sided). **c,** Each dot represents one biologically independent tumor sample. (n= 6, 5, 3 respectively, from left to right in each graph) Student's t-tests were performed (two-sided). **g & h,** Data is from at least two biological replicates (n=3 for WT and n=2 for *Sirt6* cKO), presented by mean.

Extended Data Figure 5, b, Each dot represents one biologically independent sample, presented by mean and S.D. (n=9 for S6HY and n=16 for S6WT). Student's t-tests were performed (two-sided). **c & e,** Data is from three biological replicates. **d,** Data is from three biological replicates.

Extended Data Figure 6, b, Data is from two independent experiments with two experimental replicates. Student's t-tests were performed (two-sided). **c,** Immunostaining was performed three times with similar results. **d,** Immunostaining was performed three times with similar results. **e,** Data is from three independent experiments with two experimental replicates. Student's t-tests were performed (two-sided). **f-h,** Data is from four biological replicates. Student's t-tests were performed (two-sided). **i,** Each dot represents one biologically independent sample, presented

by mean and S.D. (n=14 for shCtrl and n=14 for shSIRT6). Student's t-tests were performed (two-sided). **j,** Data is from three biological replicates. **k,** Data is from two independent experiments with two experimental replicates. Student's t-tests were performed (two-sided). **l & m,** Data is from at least two biological replicates (n=2 for shCtrl and n=3 for shSIRT6).

Extended Data Figure 7, a, Data is from three independent experiments (n=10 each sample). Student's t-tests were performed (two-sided). **b,** Data is from three independent experiments. Two-way ANOVA test was performed. **d,** Two-way ANOVA test was performed. **e,** Immunostaining was performed two times with similar results.

Extended Data Figure 8, a, Data is always reproducible every time the code was run. The key point for this stability is the random seed point in the t-SNE algorithm is set to zero and that maintained reproducibility. The t-SNE analysis was done on MATLAB 2018a that was installed on a workstation operating with Windows 10. **c & e,** Data is from two biologically independent tumor samples, consisting of more than hundred thousands of pixel datapoints per sample. **d & f,** The nonparametric Wilcoxon rank sum test (two-sided and 95% significance level) was used after checking normality distribution using Kolmogorov-Smirnov test. Details of the box plots are listed in the

Source Data file 4. **g,** Data is from two biologically independent tumor samples, consisting of more than hundred thousands of pixel datapoints per sample. **h,** Data is always reproducible every time the code was run. The key point for this stability is the random seed point in the t-SNE algorithm is set to zero and that maintained reproducibility. The t-SNE analysis was done on MATLAB 2018a that was installed on a workstation operating with Windows 10.

Extended Data Figure 10, a, Each dot represents one biologically independent tumor sample. (n= 5, 3, 10, 7, respectively, from left to right in each graph) Student's t-tests were performed (two-sided). **b,** Bright field imaging was performed two times with similar results.

Supplementary Table 6, To be considered a marker gene, the gene must be enriched in the given cluster with a Wilcoxon Rank Sum test Bonferroni-adjusted p-value of less than 0.05 and a minimum log-fold change of 0.25 when comparing the cells of the cluster to all other cells. Statistical analysis was performed in R (version 3.6.1).

Reporting Summary

Further information on research design is available in the Nature Research Reporting Summary linked to this article.

Data availability

The RNA-seq data of the tumor subpopulations from mouse cutaneous tumors of Sirt6 WT or cKO animals have been submitted to the Gene Expression Omnibus (GEO) database under accession number GSE115953 (Related to Fig. 2d-f and Extended Data Fig. 4e-h). The scRNA-seq data of tumor-propagating cells from mouse cutaneous tumors of Sirt6 WT or cKO animals have been submitted to the Gene Expression Omnibus (GEO) database under accession number GSE147031 (Related to Fig. 4b-e and Extended Data Fig. 9a-j). There is no restriction on data availability. Human HNSCC scRNA-seq data from Puram S.V. et al. is available in GSE103322 (Related to Fig. 4h and Extended Data Fig. 10c-d). Oncomine and TCGA dataset (Related to Extended Data Fig.1a-c & 2e) is available in cBioportal (cbioportal.org). Cancer Cell Line Encyclopedia data (Related to Extended Data Fig.1e) is available in portals.broadinstitute.org/ccle. Source Data are provided with this article.

Code availability

All the in-house codes were previously used in the published works. Appropriate references to the original works have been included.

Correspondence and request of materials should be addressed to Raul Mostoslavsky.

REFERENCES for METHODS

30. Rhodes, D. R. *et al.* Oncomine 3.0: genes, pathways, and networks in a collection of 18,000 cancer gene expression profiles. *Neoplasia (New York, N.Y.)* **9,** 166–180 (2007).
31. Barretina, J. *et al.* The Cancer Cell Line Encyclopedia enables predictive modelling of anticancer drug sensitivity. *Nature* **483,** 603–607 (2012).
32. Lawrence, M. S. *et al.* Comprehensive genomic characterization of head and neck squamous cell carcinomas. *Nature* **517,** 576–582 (2015).
33. Fitamant, J. *et al.* YAP Inhibition Restores Hepatocyte Differentiation in Advanced HCC, Leading to Tumor Regression. *Cell reports* **10,** 1692–1707 (2015).
34. Dobin, A. *et al.* STAR: ultrafast universal RNA-seq aligner. *Bioinformatics* **29,** 15–21 (2013).
35. Anders, S., Pyl, P. T. & Huber, W. HTSeq--a Python framework to work with high-throughput sequencing data. *Bioinformatics* **31,** 166–169 (2015).
36. Robinson, M. D., McCarthy, D. J. & Smyth, G. K. edgeR: a Bioconductor package for differential expression analysis of digital gene expression data. *Bioinformatics* **26,** 139–140 (2010).
37. Subramanian, A. *et al.* Gene set enrichment analysis: a knowledge-based approach for interpreting genome-wide expression profiles. *Proc Natl Acad Sci USA* **102,** 15545–15550 (2005).

38. Donner, A. J., Szostek, S., Hoover, J. M. & Espinosa, J. M. CDK8 Is a Stimulus-Specific Positive Coregulator of p53 Target Genes. *Molecular Cell* **27,** 121–133 (2007).
39. Heinrich, P. *et al.* Correcting for natural isotope abundance and tracer impurity in MS-, MS/MS- and high-resolution-multiple-tracer-data from stable isotope labeling experiments with IsoCorrectoR. *Sci. Rep.* **8,** 17910 (2018).
40. Elia, I. *et al.* Breast cancer cells rely on environmental pyruvate to shape the metastatic niche. *Nature* **568,** 117–121 (2019).
41. Young, J. D., Walther, J. L., Antoniewicz, M. R., Yoo, H. & Stephanopoulos, G. An elementary metabolite unit (EMU) based method of isotopically nonstationary flux analysis. *Biotechnol. Bioeng.* **99,** 686–699 (2008).
42. Abdelmoula, W. M. *et al.* Automatic generic registration of mass spectrometry imaging data to histology using nonlinear stochastic embedding. *Anal. Chem.* **86,** 9204–9211 (2014).
43. Klein, S., Staring, M., Murphy, K., Viergever, M. A. & Pluim, J. P. W. elastix: a toolbox for intensity-based medical image registration. *IEEE Trans Med Imaging* **29,** 196–205 (2010).
44. Viola, P. & Wells, W. M., III. Alignment by Maximization of Mutual Information. *International Journal of Computer Vision* **24,** 137–154 (1997).
45. Klein, S., Staring, M., Andersson, P. & Pluim, J. P. W. Preconditioned stochastic gradient descent optimisation for monomodal image registration. *Med Image Comput Comput Assist Interv* **14,** 549–556 (2011).
46. Thévenaz, P., Ruttimann, U. E. & Unser, M. A Pyramid Approach to Subpixel Registration Based on Intensity. *IEEE transactions on image processing : a publication of the IEEE Signal Processing Society* **7,** (1998).
47. Abdelmoula, W. M. *et al.* Automatic generic registration of mass spectrometry imaging data to histology using nonlinear stochastic embedding. *Anal. Chem.* **86,** 9204–9211 (2014).
48. Sade-Feldman, M. *et al.* Defining T Cell States Associated with Response to Checkpoint Immunotherapy in Melanoma. *Cell* **176,** 404 (2019).
49. Li, B. & Dewey, C. N. RSEM: accurate transcript quantification from RNA-Seq data with or without a reference genome. *BMC Bioinformatics* **12,** 323 (2011).
50. Ilicic, T. *et al.* Classification of low quality cells from single-cell RNA-seq data. *Genome Biol* **17,** 29 (2016).

51. Stuart, T. *et al.* Comprehensive Integration of Single-Cell Data. *Cell* **177,** 1888–1902.e21 (2019).
52. Qiu, X. *et al.* Reversed graph embedding resolves complex single-cell trajectories. *Nat Meth* **14,** 979–982 (2017).

Fig. 1.

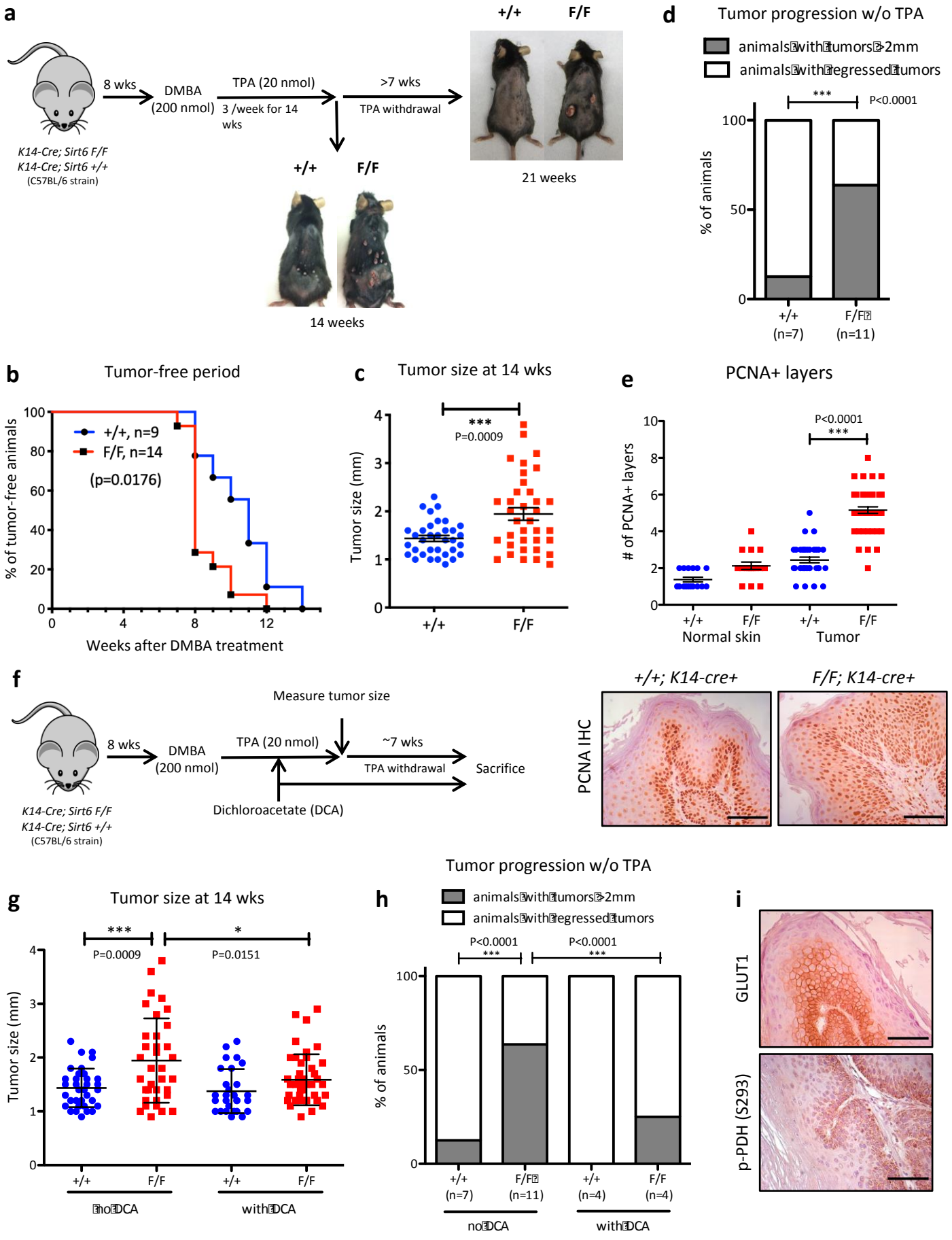
a
8 wks
DMBA (200 nmol)
TPA (20 nmol) 3 /week for 14 wks
>7 wks TPA withdrawal
K14-Cre; Sirt6 F/F
K14-Cre; Sirt6 +/+
(C57BL/6 strain)
+/+
F/F
21 weeks
14 weeks
d
Tumor progression w/o TPA
animals with tumors ≥2mm
animals with regressed tumors
***
P<0.0001
% of animals
+/+ (n=7)
F/F (n=11)
b
Tumor-free period
+/+, n=9
F/F, n=14
(p=0.0176)
% of tumor-free animals
Weeks after DMBA treatment
c
Tumor size at 14 wks
***
P=0.0009
Tumor size (mm)
e
PCNA+ layers
P<0.0001
***
# of PCNA+ layers
Normal skin
Tumor
f
Measure tumor size
8 wks
DMBA (200 nmol)
TPA (20 nmol)
~7 wks
TPA withdrawal
Sacrifice
Dichloroacetate (DCA)
K14-Cre; Sirt6 F/F
K14-Cre; Sirt6 +/+
(C57BL/6 strain)
+/+; K14-cre+
F/F; K14-cre+
PCNA IHC
g
Tumor size at 14 wks
***
P=0.0009
*
P=0.0151
Tumor size (mm)
no DCA
with DCA
h
Tumor progression w/o TPA
animals with tumors ≥2mm
animals with regressed tumors
P<0.0001
***
P<0.0001
***
% of animals
+/+ (n=7)
F/F (n=11)
+/+ (n=4)
F/F (n=4)
no DCA
with DCA
i
GLUT1
p-PDH (S293)

Fig. 2.

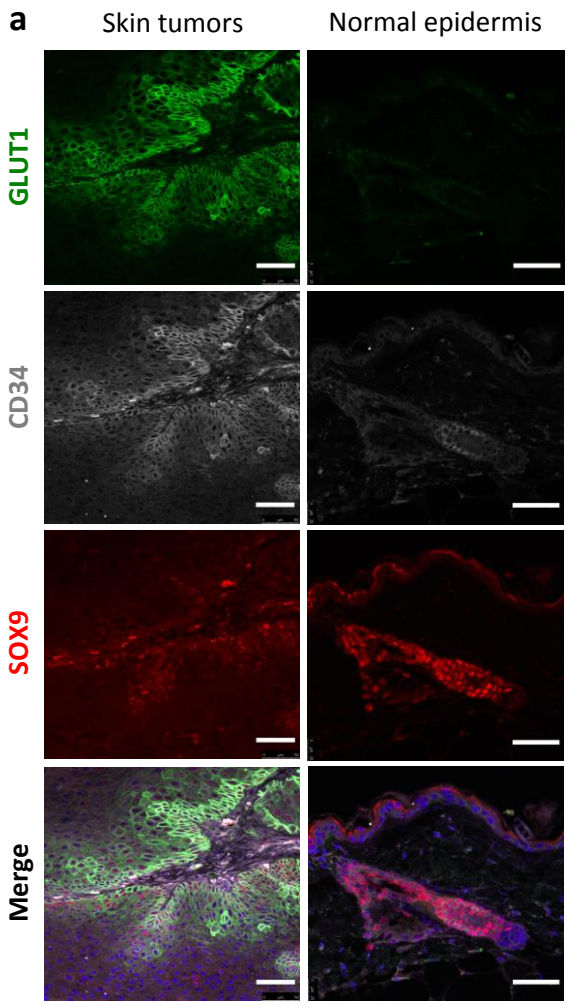

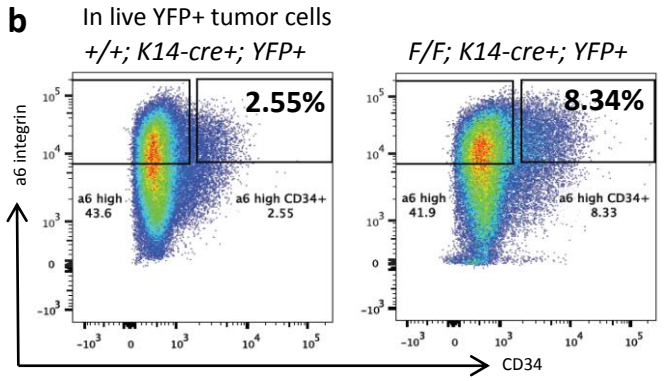

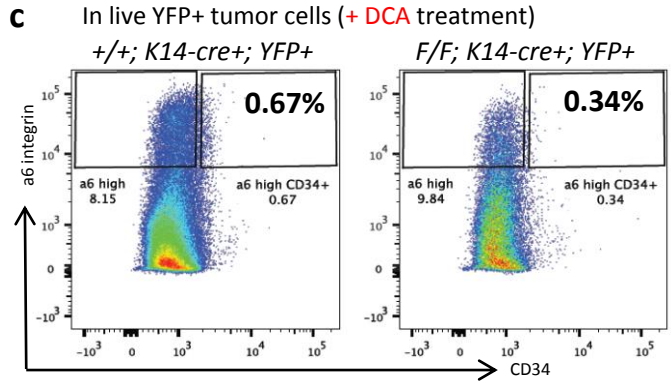

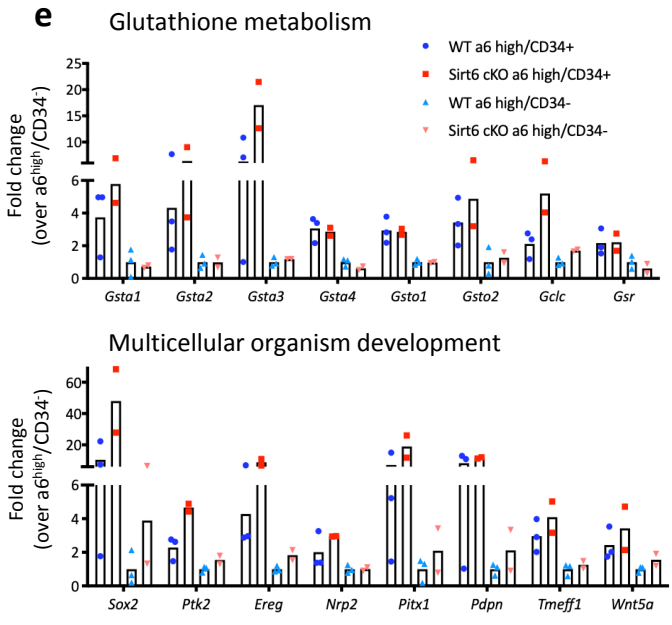

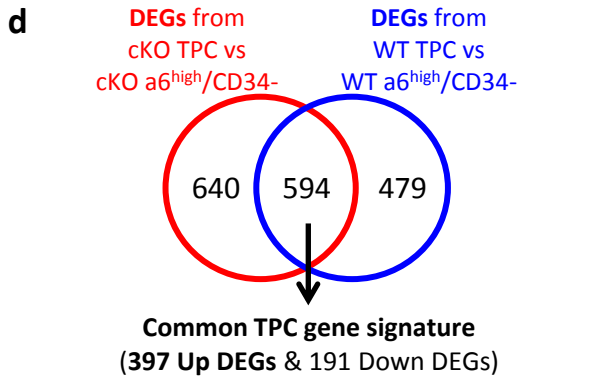

Biological process (GOTERM_BP_DIRECT)	p value
Keratinization	6.70E-11
Glutathione metabolic process	2.80E-05
Amino acid transport	1.10E-04
Lipid metabolic process	2.00E-03
Cell fate commitment	2.00E-03
Multicellular organism development	7.90E-03
Epidermal growth factor receptor signaling pathway	9.00E-03

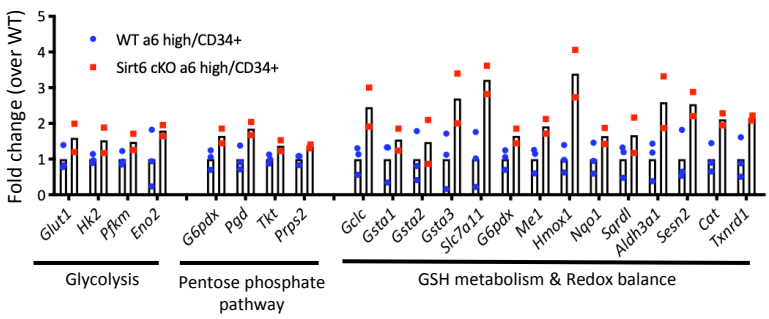

Fig. 3.

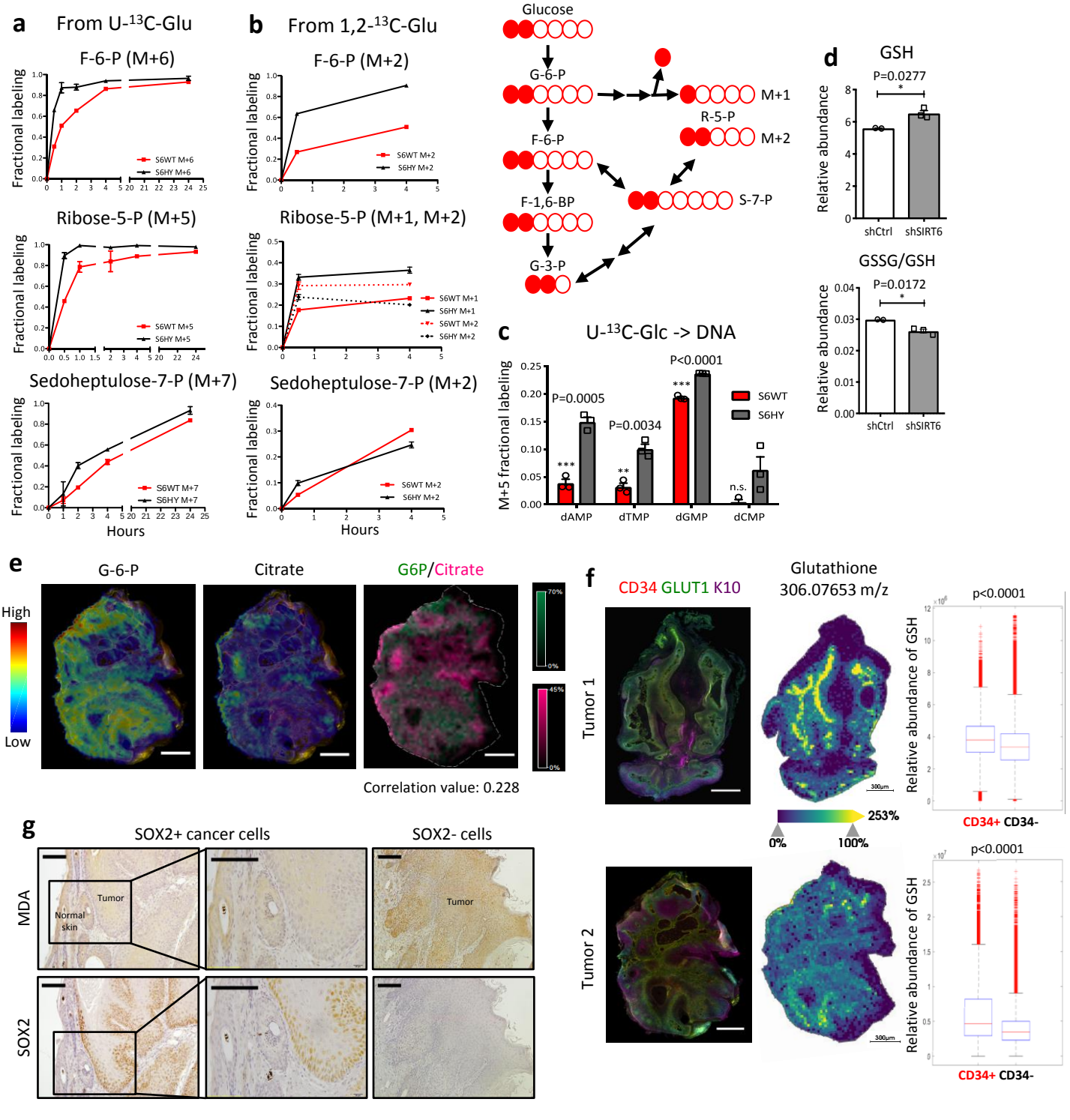
a
From U-13C-Glu
F-6-P (M+6)
S6WT M+6
S6HY M+6
Ribose-5-P (M+5)
S6WT M+5
S6HY M+5
Sedoheptulose-7-P (M+7)
S6WT M+7
S6HY M+7
Fractional labeling
Hours
b
From 1,2-13C-Glu
F-6-P (M+2)
S6WT M+2
S6HY M+2
Ribose-5-P (M+1, M+2)
S6WT M+1
S6HY M+1
S6WT M+2
S6HY M+2
Sedoheptulose-7-P (M+2)
Glucose
G-6-P
F-6-P
F-1,6-BP
G-3-P
R-5-P
S-7-P
M+1
M+2
c
U-13C-Glc -> DNA
M+5 fractional labeling
P=0.0005
P=0.0034
P<0.0001
n.s.
S6WT
S6HY
dAMP
dTMP
dGMP
dCMP
d
GSH
P=0.0277
Relative abundance
shCtrl
shSIRT6
GSSG/GSH
P=0.0172

e
G-6-P
Citrate
G6P/Citrate
High
Low
Correlation value: 0.228

f
CD34 GLUT1 K10
Glutathione
306.07653 m/z
Tumor 1
Tumor 2
253%
0%
100%
p<0.0001
Relative abundance of GSH
CD34+ CD34-

g
SOX2+ cancer cells
SOX2- cells
MDA
SOX2
Tumor
Normal skin

Fig. 4.

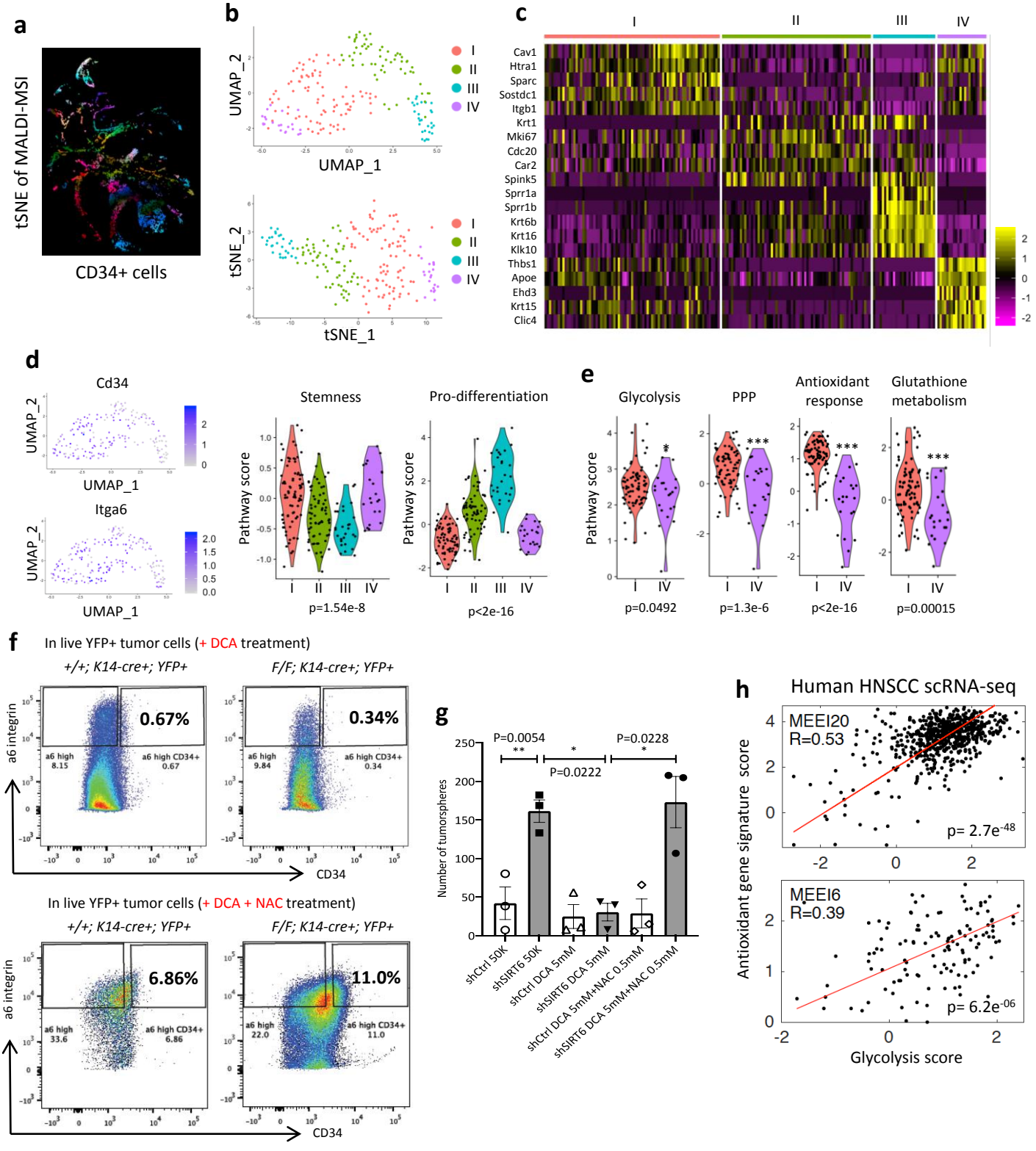
a
tSNE of MALDI-MSI
CD34+ cells
b
UMAP_2
UMAP_1
tSNE_2
tSNE_1
I
II
III
IV
c
Cav1
Htra1
Sparc
Sostdc1
Itgb1
Krt1
Mki67
Cdc20
Car2
Spink5
Sprr1a
Sprr1b
Krt6b
Krt16
Klk10
Thbs1
Apoe
Ehd3
Krt15
Clic4
d
Cd34
Itga6
Stemness
Pro-differentiation
Pathway score
p=1.54e-8
p<2e-16
e
Glycolysis
PPP
Antioxidant response
Glutathione metabolism
p=0.0492
p=1.3e-6
p<2e-16
p=0.00015
f
In live YFP+ tumor cells (+ DCA treatment)
+/+; K14-cre+; YFP+
F/F; K14-cre+; YFP+
0.67%
0.34%
a6 integrin
CD34
In live YFP+ tumor cells (+ DCA + NAC treatment)
6.86%
11.0%
g
Number of tumorspheres
P=0.0054
P=0.0222
P=0.0228
shCtrl 50K
shSIRT6 50K
shCtrl DCA 5mM
shSIRT6 DCA 5mM
shCtrl DCA 5mM+NAC 0.5mM
shSIRT6 DCA 5mM+NAC 0.5mM
h
Human HNSCC scRNA-seq
MEEI20
R=0.53
p= 2.7e-48
MEEI6
R=0.39
p= 6.2e-06
Antioxidant gene signature score
Glycolysis score